TAMPEREEN TEKNILLINEN YLIOPISTO
TAMPERE UNIVERSITY OF TECHNOLOGY

Amandeep Singh

Green synthesis of TiO_2 nanoparticles and carbon nanotubes by pulsed laser ablation of titanium and graphite in deionised water

Master of Science Thesis

Examiners: Professor Erkki Levänen, Doctoral Student Erkka Frankberg and Research Manager Jorma Vihinen

Examiners and topic approved by the Council of the Faculty of Engineering Sciences on 8th October, 2014

ABSTRACT

TAMPERE UNIVERSITY OF TECHNOLOGY
Master's Degree Programme in Materials Science Engineering
SINGH, AMANDEEP: Green synthesis of TiO_2 nanoparticles and carbon nanotubes by pulsed laser ablation of titanium and graphite in deionised water.

Master of Science Thesis, 72 pages
November 2014
Major: Materials Technology
Examiner: Professor Erkki Levänen, Doctoral Student Erkka Frankberg and Research Manager Jorma Vihinen
Keywords: Pulsed laser ablation; Nanoparticles, Titanium, Graphite, Diamond, Anatase, Brookite, Rutile, TiO_2, Carbon nanotubes, Pulsed laser ablation in liquid, Transmission electron microscopy, Energy dispersive x-ray spectroscopy, X-ray diffraction, Small angle x-ray scattering, Laser fluence.

The thesis is divided into three sections: Background of the study, experimental, and finally discussion. The first part includes the literature survey which discusses the studies related to pulsed laser ablation that have been reported so far in the state-of-the-art. From the second part, the reader can study the fundamentals of the experimental methods used in order to understand the results. The third part of the thesis consists of the results from this study and a discussion on them followed by the conclusions for this thesis project.

In this study, green synthesis of TiO_2 nanoparticles and carbon nanotubes was successfully demonstrated through pulsed laser ablation in deionised water. The nanoparticle yield for ablated titanium suspensions was found to increase with laser fluence till 40% laser power and then decrease at 50% laser power due to reduced laser fluence but again increase at 60% laser power due to overlapping of laser spots. The yield of nanoparticles in ablated graphite suspensions was independent of laser fluence but proportional to laser power until the power was so high that evaporation of liquid interfered and decreased the yield. The transmission electron microscopy of suspensions from ablated titanium target revealed round crystalline TiO_2 nanoparticles surrounded by amorphous phase nanoparticles. X-ray diffraction and wide angle x-ray scattering of these nanoparticles confirmed presence of anatase, rutile and brookite. For ablated titanium target, x-ray diffraction detected titanium monoxide, titanium dioxide and titanium (III) oxide besides titanium metal. The particle size measurements from TEM and SAXS indicated decrease in the average size of TiO_2 nanoparticle with the increase in laser power. The transmission electron microscopy of the suspensions from ablated graphite target indicated the presence of carbon nanotubes. X-ray diffraction of the ablated graphite target detected the presence of diamond on the target surface.

PREFACE

It is exciting for any material scientist to think about the idea of interaction of lasers and matter to synthesise nanoparticles but it is even more thrilling to see this idea transform into a full-fledged thesis now.

It is with immense pleasure that I thank Erkki Levänen for not only giving me the opportunity to pursue this excellent and challenging thesis topic with the ceramic materials group at Tampere University of Technology but also for believing in my abilities to do state-of-the-art research and for the helpful discussions. I would like to acknowledge Erkka Frankberg for all the discussions, plans, ideas, brainstorming and intensive writing sessions during weekdays and weekends. Many thanks to the people who helped with the experiments and characterisations: Jorma Vihinen for experiments with laser and guidance for thesis, Mari Honkanen for transmission electron microscopy, Leo Hyvärinen for x-ray diffraction. Also special thanks to Matti Järveläinen for his help and support during this study.

I would like to thank my parents and my brother for the much needed support and for boosting my morale.

Also many thanks to Eveliina Sippola, Saara Heinonen, Aaretti Kaleva, Arnold Ismailov and to all my co-workers in the ceramics laboratory, surface engineering laboratory, and in materials science department for their assistance during this thesis study.

TABLE OF CONTENTS

SYMBOLS AND ABBREVIATIONS

S.I. Units

J	Joules
m	Meter
s	Second
K	Kelvin
Hz	Hertz
Pa	Pascal
W	Watts

Abbreviations

TiO	Titanium monoxide
TiO_2	Titanium dioxide
Ti_2O_3	Titanium (III) oxide
EDS	Energy dispersive x-ray spectrometry
LP-PLA	Liquid phase pulsed laser ablation
PLA	Pulsed Laser Ablation
PLAL	Pulsed Laser Ablation in Liquid
SAXS	Small angle x-ray scattering
TEM	Transmission electron microscopy
WAXS	Wide angle x-ray scattering
XRD	X-ray diffraction

Greek symbols

α	Absorption coefficient
δ	Optical penetration depth
μ_v	Attenuation coefficient

Alphabetic

I_v	Intensity of transmitted radiation
I_{vo}	Intensity of incident radiation
x	Path length of transmitted laser beam

1. INTRODUCTION

Nanotechnology has remarkably revolutionised the technology sector in terms of the advancements in engineering, biomedical sciences, energy sector, health care and power sector. It involves the analysis and manipulation of materials at the atomic scale. Nanotechnology has been the centre of attraction for physicists, chemists and material scientists from the few decades. A new era in nanotechnology began with the discovery of graphene in 2004 by Andre Geim and Konstantin Novoselov [1]. A significant fraction of nanotechnology deals with the production of nanoparticles. It includes synthesis and processing of nanoparticles of metals, metal oxides, metal carbides, semi-conductors, and carbon nanoparticles. The global nanoparticle market is rapidly increasing and will exceed US $6 billion by 2016 (estimated 23% growth for next five years) [2]. The market for graphene has been projected to increase from $20 million in 2014 to more than $390 million in 2024 [3]. The European Union has already dedicated €1 Billion for the 'Graphene Flagship' project. These statistics suggest the extensive potential market of nanomaterials.

The prevalent methods of production of nanomaterials such as graphene are chemical vapour deposition and chemical exfoliation which are toxic and batch type processes [4]. As they involved toxic chemical, therefore, they are hazardous and environmentally destructive. In addition, the nanoparticles obtained by traditional methods are of low purity, therefore, further functionalization of those nanoparticles is not possible. Other issues with the traditional methods is that they are difficult to scale up.

Pulsed laser ablation in liquids offers green synthesis of nanoparticles without forming any by-products [5]. The removal of material from target surface due to irradiation with ultra-short laser leads to formation of high temperature plasma, which is known as pulsed laser ablation [6]. Recently researcher have reported synthesis of pure metal nanoparticles, metal oxide nanoparticles and metal carbide nanoparticles [7–12]. Yang et al. [13] have reported synthesis of nanocrystalline diamond with this technique. However, little research has been done on studying the total effect of laser fluence and laser power on the synthesis of TiO_2 and carbon nanoparticles by pulsed laser ablation in liquids. Also, the effect of laser parameters on the synthesis yield and on the particle shape, size, and size distribution is presently inconclusive. In addition, the characterisation of the ablated target is not well reported.

The first aim of this thesis study is production of nanoparticles directly to solution by pulsed laser ablation of titanium and graphite in deionised water. This will enable fast and simple production of particles, and it also allows possibility of wet stage processing of the synthesised nanoparticles later, such as, dispersion and colloidal processing. The nanoparticles synthesised by this method are well suited for functionalization [14].

The second aim of the study is to analyse the effect of laser power and laser fluence on the synthesised nanoparticles in terms of variation in their size, or shape, or size

distribution. The third aim of this study is to study the laser ablated targets. The final aim of this study is to study the effect of laser power and laser fluence on the yield of the synthesised nanoparticles by pulsed laser ablation in deionised water.

2. THEORETICAL BACKGROUND

This chapter discusses important parameters of lasers, the fundamentals of pulsed laser ablation process and pulsed laser ablation process in liquid. Furthermore the mechanism of nanoparticle formation in pulsed laser ablation in liquids and the interaction of laser beam with solid target has been explained. This chapter provides the background to analyse the results and to understand the discussion in Chapter-4.

2.1 Laser and its parameters

Lasers have the advantage of providing a very high energy density on the target which results in very high local temperatures. Therefore, the processes which are otherwise thermodynamically not possible or metastable phases of materials which can otherwise not be formed, are possible with the help of laser processing. Laser fluence is the energy per unit area [J/cm^2] on the target surface. The maximum energy per pulse and the spot diameter of the beam determines the maximum laser fluence possible with a laser. Other extremely important parameter of a pulsed laser is its pulse repetition rate and the pulse length. The repetition rate varies from a few Hz to several MHz. Depending on the pulse length, there are different lasers available such as nanosecond lasers, picosecond lasers, and femtosecond lasers, which indicates the longevity of a single pulse in time units. These are the most commonly used laser types for pulsed laser ablation experiments.

2.2 Pulsed Laser Ablation

The formation of a high-temperature, ultra-dense plasma when a focussed beam of laser (extremely short pulse length 10^{-15} to 10^{-9} s) irradiates a solid target is known as pulsed laser ablation (PLA) [6]. Laser ablation can also be defined as the ejection of target material from its surface by ultra-short laser pulses when the surface is irradiated with it [10]. As a wide variety of materials can be synthesised with PLA, it has captivated great deal of attention [6]. Pulsed laser ablation can be carried out in gas or liquid or vacuum. This process of nanoparticle synthesis is a bottom-up method, in which the desired materials are synthesised by incorporation of smaller material fragments such as nanoparticles. Pulsed laser ablation in gaseous atmosphere and vacuum, known as pulsed laser deposition, has been widely reported and is an established method for producing thin films [15]. A modification of this process is pulsed laser ablation in liquids to produce nanoparticles, which involves the advantages of the standard pulsed laser ablation process as well as being a green processing method. This process does not involve any chemicals for the synthesis of nanoparticles and it is environment friendly since there is no emission of hazardous and toxic gases. The nanoparticles produced are obtained in the form of a colloidal suspension which also improves safety compared to dry processed nanopowders.

2.3 Pulsed laser ablation in liquids

Pulsed laser ablation of a target while immersed in liquid is termed pulsed laser ablation in liquid (PLAL). Liquid phase pulsed laser ablation (LP-PLA same as PLAL) is a modern materials processing technique that is not just less expensive and easier to use but it also does not lead to production of any unintended reaction products [15]. T. Sasaki et al. [5] described pulsed laser ablation in liquid as a unique and excellent technique for synthesising nanoparticles. The basic experimental set-up of a pulsed laser ablation experiment in shown in figure 2.1.

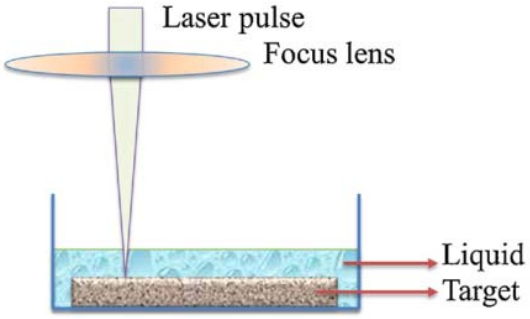

Figure 2.1 *The basic experimental set-up of pulsed laser ablation in liquid.* [10]

The experimental set-up of a liquid phase pulsed laser ablation process consists of a laser, focussing lens, target, liquid and a test vessel. Liquid phase pulsed laser ablation (LP-PLA) process has been successfully utilised to synthesise pure metals nanoparticles, metal oxide nanoparticles and metal carbide nanoparticles [7–12]. Furthermore, this technique has been used to successfully produce carbon nanotubes, carbon nanoparticles, nanodiamonds, diamond nanocrystals and higher order diamondoids [13, 15–17]. Kazakevich et al. [18] have reported the synthesis of gold-silver and silver-copper alloyed nanoparticles. This method has been reported as an alternative for the synthesis of active metal nanoparticles [19]. Moreover, functionalization of the nanoparticles such as synthesis of silica coated gold nanoparticles has also been demonstrated [14]. The plasma and cavitation bubbles formed during PLA in fluids serve as the reaction field for the synthesis of nanoparticles [20].

2.4 Mechanism of nanoparticle formation in liquid phase pulsed laser ablation

Ibrahimkutty et al. [21] have explained the basic mechanism of nanoparticle formation with the pulsed laser ablation process in liquids. Figure 2.1 [14] shows the step-wise nanoparticle formation process in pulsed laser ablation in liquids. The first stage includes irradiation of the target with the laser which gives rise to the high temperature plasma that

produces a shockwave and a bubble that expands in the second stage. The third stage involves nucleation of the nanoparticles as a result of the sudden quenching of the plasma that expanded inside the bubble. This is followed by release of nanoparticles in surrounding liquid when the bubble collapses in the fourth stage. In the final stage, ions and atoms join together to form small particles. The advantage of pulsed laser ablation in liquid is that firstly it does not require a vacuum environment, so it is relatively cheap to conduct, and secondly by-products are not formed [5]. Moreover, the synthesised nanoparticles are free from impurities and appropriate for additional processing such as functionalization [14]. The size of the nanoparticles and the agglomeration can be controlled by adding surfactants that have the ability to modify the surface charge of particles [5].

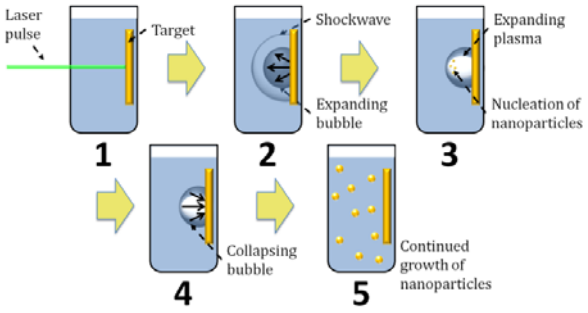

Figure 2.2 *The step-wise nanoparticle formation process in pulsed laser ablation in liquid* [14].

Semaltianos et al. [12] had used this method to synthesise titanium monoxide nanoparticles from a titanium target. Figure 2.3 shows the schematic of the physical mechanism that they had proposed. The presence of liquid in PLAL complicates the process as the expanding plasma plume is confined by the liquid, there is increased pressure and the water plasma plume also tries to compress the titanium plasma plume. This leads to a shockwave at the interface of the plasma plume and the liquid. The ultra-high pressures and temperatures thus created lead to formation of metastable phases due to favourable thermodynamics. These metastable phases freeze-out upon quenching of the plasma species and then form nanoparticles of the metastable state.

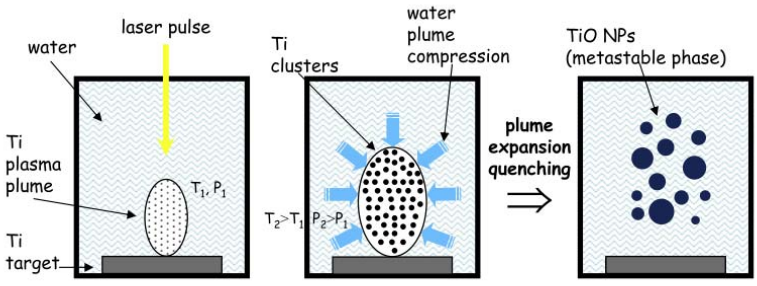

Figure 2.3 *Formation of TiO nanoparticles by physical mechanism.* [12]

The advantages of PLAL process are that the cost of processing is low, process implementation is easy and no by-products are formed. Other advantages include control on functionalization of particles and on their size and morphology [16]. With this method, huge amounts of materials can be ablated from the target and particles containing atoms from target as well as solvent can be produced [13]. In liquid phase pulsed laser ablation, we obtain the nanoparticles as a suspension, which results in added advantage that the nanoparticles are easily collected.

2.5 Phenomena occurring during interaction of pulsed laser with a solid target in liquid

Ablation happens when the intensity of the laser beam on the target surface is greater than the threshold laser fluence of the target material. There are several parameters that control the properties of the desired product such as the laser parameters, type of liquid used, the target material properties, and the interaction of laser with the target in liquid. The attenuation of laser beam, which is the decrease in the intensity of laser beam as it passes through the liquid, is also one such parameter.

Pulsed laser ablation in liquids induces a reaction field of high temperature (approximately 10^4K) and high pressure (approximately 1 GPa). This unique reaction field is believed to support the formation of nanoparticles [22]. This reaction field gives rise to emission of shock waves, formation of cavitation bubbles and their collapse, and also affects the nanocluster formation. It is important to understand these phenomenon before proceeding to the next chapter.

2.5.1 Shock wave emission

The sudden change in the flow variables, such as density, is termed as shock wave. The laser beam passes through the liquid and irradiates the surface of the target which leads to surplus energy on the target surface. This excess energy is relaxed through the emission of shock waves. Using shadowgraph imaging, Yan et al. [10] reported that acoustic cavitation led to the formation of cavitation bubbles formed in the path of the laser beam. It was further reported that the propagation of the shock wave consumes a substantial amount of laser power [10].

2.5.2 Attenuation of laser beam in liquid

For the effect of liquid on the intensity of the laser beam as it passes through the liquid, Yan et al., have discussed two relations that are discussed below.

1. The laser beam gets attenuated as it goes past the liquid because the photons get absorbed or scatter by the liquid and surfactant molecules, also by ions and particles from earlier laser pulses. The exponential decrease in the intensity is according to the following relation

$$I_v = I_{vO}\, exp\left[-\int_0^x \mu_v dx\right] \quad (1)$$

where I_v and I_{vo} are the intensities of the transmitted and incident radiation respectively, μ_v is attenuation coefficient (consists of absorption coefficient α), and x is the path length.

2. The attenuation can be stated in terms of Lambert-Beer law in cases where absorption dominates according to the following relation

$$I_v = I_{v0}\, exp^{(-\alpha x)} \quad (2)$$

The absorption coefficient (α) and the optical penetration depth (δ) in an absorbing material are related to by the following expression

$$\delta = 1/\alpha \quad (3)$$

The particles synthesised during the pulsed laser ablation experiment considerably attenuate the laser beam if ablation is carried out for long durations. This results in greater concentration of particles. This effect is even more pronounced in nanoparticles of metals. This absorption of laser energy leads to secondary processing of the nanoparticles by the laser. Takami et al. [23] have reported decrease in the particle size due to melting and vaporisation effects induced by laser.

2.5.3 Variation in the focal length of laser in liquid

In the pulsed laser ablation experiment in liquids, the refraction of the laser beam occurs due to higher refractive index of the liquids used as compared to when no solvent is present. Due to refraction, the focal length of the laser beam will change.

2.5.4 Formation of laser induced bubbles

The formation of bubbles at the target-liquid interface is a characteristic feature of liquid phase pulsed laser ablation process. Bubbles form either due to explosive boiling of the liquid or due to cavitation. The lifetime of these bubbles is dependent on the liquid viscosity. If the liquid viscosity is increased, the lifetime of the bubble increases. This is because of decrease in the rates of bubble growth and bubble collapse [10].

2.5.5 Formation of nanoclusters

The rapid cooling of the ablation plume upon expansion of the bubbles formed by laser leads to the combination of ablated ions and electrons present in the plasma. The nucleating critical clusters and growing nuclei constitute the condensation process. Tillack et al. [24] have reported decrease in the average cluster size when ions are present in the ablation plume as it increases the nucleation rate.

3. RESEARCH METHODS AND MATERIALS

This section covers the processing of the nanoparticles and explains the fundamentals of the methods used for their characterisation. In the description of the methods, the basic sample preparation and the reasons for using that technique have been mentioned.

3.1 Materials used and sample preparation

Titanium (99.99% pure) in the form of plate of thickness 3 mm, length 50 mm and width 50 mm was ordered from Goodfellow Cambridge Limited. Iron (4.8 ppm) and vanadium (1.15 ppm) were present as impurities in the titanium sample. **Graphite** (99.95% pure) in the form of a rod of diameter 25 mm and length 50 mm was also ordered from Goodfellow Cambridge Limited. Both titanium and graphite samples were cut into smaller size targets by using Struers Accutom-50 precision cutter. For the experiment, only deionised water was used and no chemicals were used for the nanoparticle synthesis. The small LDPE bottles used for storing the suspensions were ordered from VWR International Limited. The bottles had a narrow round neck and were 15 ml in volume shown in figure 3.1a. The glass vials used for drying the suspensions had a maximum volume of 6 ml when filled to the brim. Figure 3.1b shows a comparison between the size of the vial and LDPE bottle.

a) **b)**

Figure 3.1 a) *The LDPE 15 ml storage bottles and* ***b)*** *A comparison between the size of LDPE bottle and glass vial.*

The 15 mm x 15 mm sized titanium targets were obtained by cutting the as received titanium plate with Struers Accutom-50 precision cutter (Figure 3.2).

Figure 3.2 *The precision cutter Struers Accutom-50 used for cutting the samples.*

As the purity of the as received titanium plate was high (99.99%), it is relatively soft metal and, therefore, no special cutting wheel was required. The top layer of the titanium target was removed by grinding and polishing on emery paper and then the titanium samples were ultrasonically cleaned. The graphite discs were cut from the graphite rod with the same precision cutter as shown in figure 3.2. The thickness of these discs were 2.25 mm and the diameter was the same as the graphite rod which was 25 mm.

3.2 Synthesis of nanoparticles

3.2.1 Pulsed laser ablation of Titanium in Deionised water

The experimental setup for this test consisted of a nanosecond 85W Nd:YAG (Neodymium doped Yttrium Aluminium Garnet) fibre laser which was available in Department of Mechanical Engineering and Industrial Systems at Tampere University of Technology, titanium targets, deionised water, test vessel, and a XY scanner for the laser. The XY scanner and the focussing of the laser beam were controlled with a computer. Jorma Vihinen was the operator of the laser. The ultrasonically cleaned target was fixed inside the test vessel at its base and then filled with deionised water (DIW) such that the thickness of the water film above the target is 5 mm. Then the target was irradiated with laser from the top perpendicular to the plane of the target.

The wavelength of the Nd:YAG laser (Figure 3.3) was 1062 nm, with a pulse length 500 ns, maximum pulse energy 3.4 mJ, and repetition rate of 25 kHz. The laser beam was focussed on the target using a lens having focal length 160 mm and the target was irradiated from perpendicular direction. The spot diameter was measured for 40%, 60%, 80% and 100% of the maximum laser power. The spot diameter varied between 50

µm and 150 µm. For lower values of laser power, it was not possible to measure the spot size.

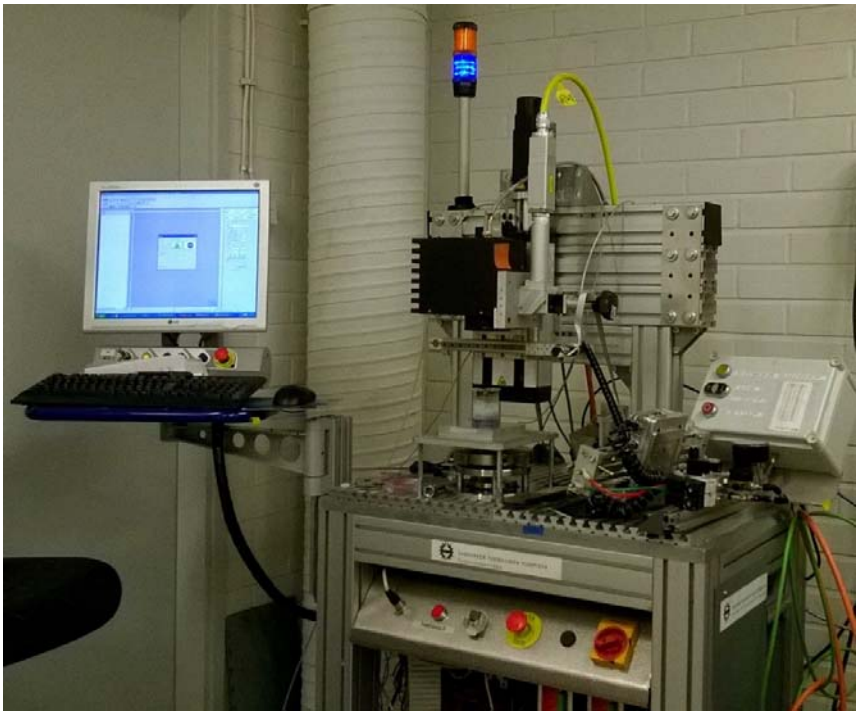

Figure 3.3 *Nd:YAG fibre laser used for pulsed laser ablation experiments is shown. The laser is connected to a XY scanner and a computer for control.*

The liquid used in this experiment was deionised water. The thickness of deionised water film above the target was 5 mm in each experiment. The laser beam was scanned over the target with the help of a scanner. The scanning speed used was 2000 mm/s. This high value of scanning speed was chosen in order to have the least number of laser pulses coincident at a point. The maximum laser fluence per pulse with this laser was 58.92 J/cm^2. The scanning area or ablated area was 8 mm X 8 mm in the pulsed laser ablation experiments. Each scanning loop was 2.566 seconds long. The number of loops were 240, 480, and 720 corresponding to Pulsed laser ablation tests of 10 minutes, 20 minutes, and 30 minutes duration respectively. The images of the titanium targets before and after ablation are shown in figure 3.4 a) and figure 3.4 b) respectively.

a) **b)**

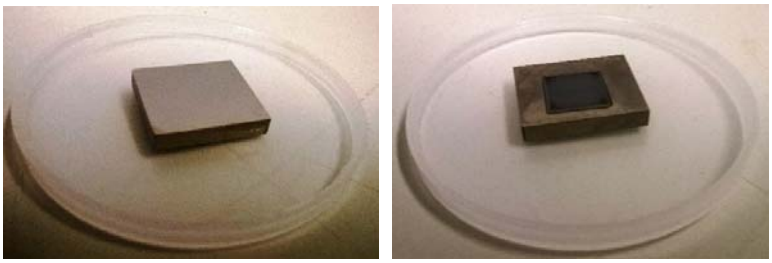

Figure 3.4 a) *As-received and cut titanium target before ablation and* ***b)*** *Pulsed laser ablated titanium target.*

3.2.2 Pulsed laser ablation of Graphite in Deionised water

The experimental set-up was the same as in case of pulsed laser ablation of titanium discussed in section **3.2.1** but in this case the target was graphite disc of diameter 25 mm and thickness 2.25 mm. Deionised water was used in the pulsed laser ablation of graphite target and the thickness of water film above the graphite target was 5 mm in each experiment. The graphite target before and after ablation is shown in figure 3.5a and figure 3.5b respectively.

a) **b)**

Figure 3.5 a) *The as-received graphite target after being cut into 2.25 mm thick disc and* ***b)*** *The graphite target after pulsed laser ablation test.*

Similar to pulsed laser ablation of titanium, in this case also, scanning speed of 2000 mm/sec was used and the scanned area was 8 mm x 8 mm. The number of loops were 480 and 720 corresponding to PLA test of 20 minutes and 30 minutes duration respectively with each scanning loop 2.566 seconds long.

3.3 Characterisation methods used for nanoparticles

3.3.1 Transmission electron microscopy

Transmission electron microscopy (TEM) was used to characterise the synthesized titanium and carbon nanoparticles. Figure 3.6 shows the TEM available with the Materials characterisation group at Materials Science Engineering Department in Tampere University of Technology that was used in this thesis project. The equipment was a JEM-2010, JEOL microscope. Mari Honkanen was the operator of this TEM. The TEM samples were carefully prepared by pipetting a few drops of the ablated suspension (in less than a minute after the ablation experiment was finished) on the carbon coated copper grid. The prepared samples were then left to dry for 24 hours in the exicator. The sample preparation for TEM was immediately done after finishing the ablation experiment so as to reduce the agglomeration effects.

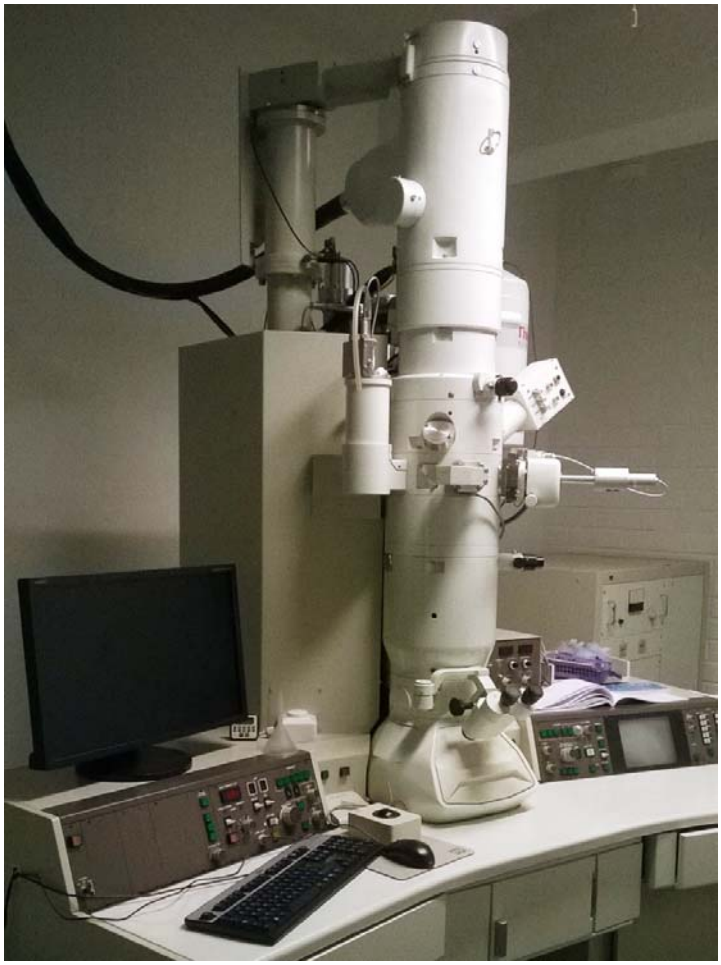

Figure 3.6 *The transmission electron microscope that was used for characterisation of pulsed laser ablated suspensions in this project.*

The images were taken at magnifications ranging from 20,000 X to 400,000 X. Electron diffraction was also performed with this TEM equipment on the same TEM samples. This was performed in order to analyse whether the nanoparticles in that region are crystalline or amorphous or nanocrystalline.

3.3.2 Energy dispersive x-ray spectroscopy

Energy dispersive x-ray spectroscopy (EDS) is a characterisation technique used for elemental analysis of electron microscopy samples. The characteristic x-rays coming from the sample are detected by the x-ray detector which converts the x-ray energy into voltage signal and then the signal is processed and amplified. In the following step, the analyser sends the digital signal to the display and we obtain different peaks for various elements in the 'Intensity versus Voltage' graph. As the ionisation energies between different energy levels of each element is distinct, therefore, we obtain discrete peaks for each element. This makes energy dispersive x-ray spectroscopy a remarkable technique for elemental analysis. The energy dispersive x-ray spectrometer connected with Transmission

electron microscope mentioned in section **3.3.1** was used in this thesis project. The samples used for this purpose were the same as the samples used for transmission electron microscopy.

3.3.3 X-ray diffraction

X-ray diffraction was used to detect the compounds and the phases present in the nanoparticle powder obtained after drying the suspensions. The drying process can be found in section **3.3.5**. This technique was also used to characterise the as received as well as the laser ablated titanium and graphite targets. This is a remarkable technique for crystal structure analysis. As it can determine the crystal structure of the element or compound present, therefore, it can be used to distinguish different polymorphs. Figure 3.7 shows the XRD equipment Panalytical Empyrean Multipurpose Diffractometer with anode material copper. For the measurements with this equipment, Leo Hyvärinen was the operator.

Figure 3.7 *The Panalytical Empyrean Multipurpose Diffractometer that was used for x-ray diffraction, wide and small angle x-ray scattering measurements.*

This equipment was capable of both qualitative as well as quantitative analysis and also small angle x-ray scattering (SAXS) and wide angle x-ray scattering (WAXS). In WAXS, the distance between the sample and the detector is smaller than in SAXS, and so, the diffraction maxima is observed at larger angles

3.3.4 Small angle x-ray scattering

Small angle x-ray scattering technique measures the scattered x-rays at very small angle ranging from 0.1° to 10°. It was used to determine the size distribution of nanoparticles in the suspensions of pulse laser ablated titanium and graphite. This technique was used also to analyse the effect of laser fluence on the size of nanoparticles and their size distribution present in the synthesized suspensions. The samples for measurement with this technique consisted of 2 ml of the pulse laser ablated suspensions. A few drops from these 2 ml samples were put in between two plastic foils that were fixed on the x-ray diffraction sample holder. Small angle x-ray scattering was performed with the x-ray diffraction machine mentioned in section 3.3.3.

3.3.5 Concentration measurements

The suspensions synthesised with pulsed laser ablation of titanium and graphite targets at different values of laser fluence were pipetted into small 15 ml bottles. 15 ml of each suspension was added in small batches of 3 ml to the corresponding vial which was kept in the oven. The weights of the vials used were measured with a weighing balance (Figure 3.8b) before beginning the drying process of suspensions. The suspensions in the vial were dried in the oven (Figure 3.8a) at 80ºC for a period of 96 hours.

a) **b)**

Figure 3.8 a) *The laser ablated suspensions were dried at 80ºC for a period of 96 hours in this oven and* ***b)*** *The weighing balance was used to measure the weights of empty vials and vials containing nanoparticle powder.*

The weight of the vial containing the dried suspension was then measured. The weight of the nanoparticle powder was calculated from the difference in the weight of empty vial and the vial containing dried suspension.

3.3.6 Surface profile measurement with optical profilometer

Optical profilometer (Veeco Instruments Inc.) was used to analyse the ablated surfaces of the titanium and graphite targets. This technique was used to measure the depth of the ablated crater on the target due to pulsed laser ablation and the overall shape of the ablated region. The images from the optical profilometer could be taken at different magnifications. The optical profilometer images were analysed using Veeco Vision software. Figure 3.9, figure 3.10 and figure 3.11 (taken from the optical profilometry of laser ablated titanium sample) show the various ways of analysis used with the Veeco Vision software. The first analysis method used was the surface dataset analyser (Figure 3.9). It gave information about the surface characteristics along with the set-up parameters used. The colour gradient and the change in colour signify the difference in elevation of the pulsed laser ablated region and the non-ablated region. In the image, the red region is the highest and the blue region is the deepest according to the colour scale.

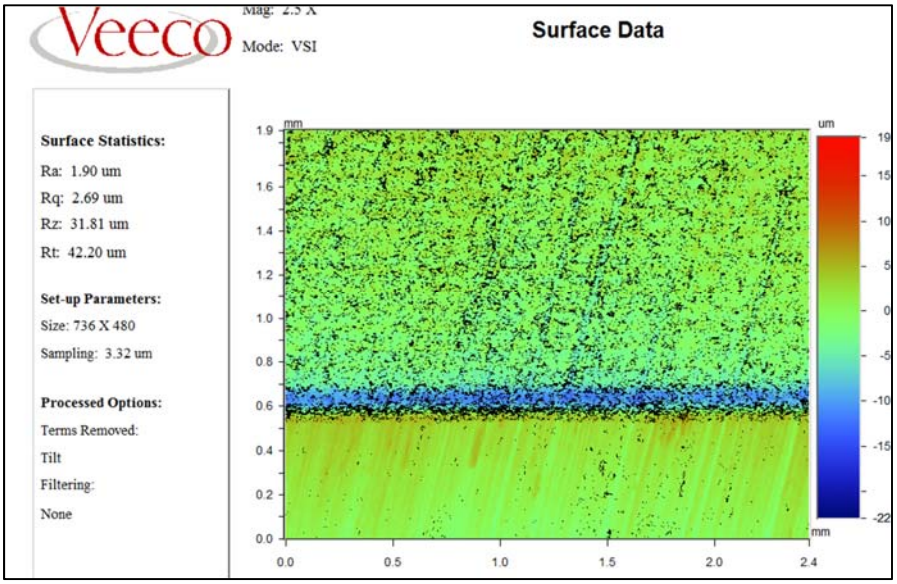

Figure 3.9 *The dataset summary view shows the set-up parameters and the surface characteristics in terms of R_a values. This 2-dimensional view of the sample surface shows the elevation calibrated with the colour scale.*

The second analysing method used was the 2-dimensional X and Y profile interface (Figure 3.10). This helped in determining the depths in the ablated region at different points and also the depth of the ablated region compared to the non-ablated region.

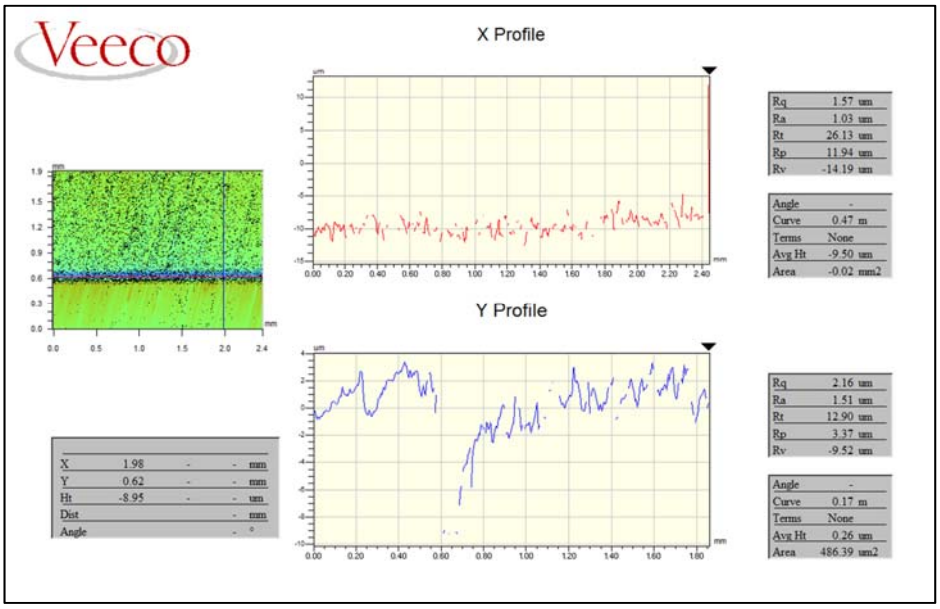

Figure 3.10 *The 2-D XY profile view shows the difference in height of the surface asperities at the point chosen. It also shows individually the X and Y profiles.*

The third analysing method was the 3-D interactive analyser (Figure 3.11) in which the surface profile of the sample is available in 3-D format and can be moved in any direction according to the sample surface characteristics. This interface helped to get an overview of the laser scanning process.

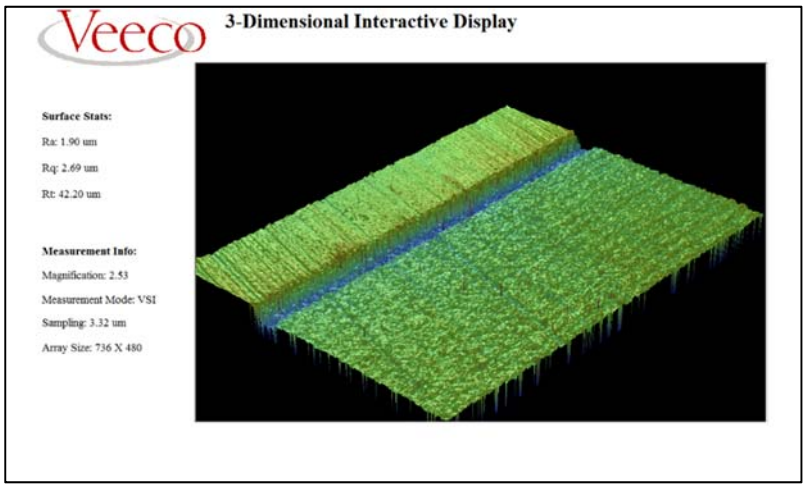

Figure 3.11 *The 3-Dimensional image of the titanium sample taken with the 3-D Interactive analyser helped to characterise the laser ablated target surface*

4. RESULTS AND DISCUSSION

In this section, initially the synthesis of nanoparticles from titanium and graphite targets by pulsed laser ablation is described and then the shape and size of the produced nanoparticles are discussed. Furthermore, the effect of total laser power and laser fluence on the amount of nanoparticles produced and on the concentration as well as agglomeration is discussed. This is followed by the characterisation of the pulsed laser ablated suspensions by transmission electron microscopy, small and wide angle x-ray scattering and x-ray diffraction. Finally, the surface profiles of the pulsed laser ablated targets are discussed to further understand how ablation changes the target surface and what is the depth of the ablated crater.

4.1 Synthesis of nanoparticles by pulsed laser ablation in deionised water

This section discusses the pulsed laser ablation of graphite and titanium in deionised water. As discussed in theory, when the targets were irradiated with the laser, the characteristic plasma was formed which signifies that the atoms and ions were ablated from the target and the ionised species form plasma. In figures 4.1a and 4.1b, the plasma formed above the target is visible which implies that the fluency of the laser is higher than the threshold fluence needed for the ablation. For titanium, plasma formation was observed at laser fluence 13.9 J/cm^2 and for graphite, it was observed at 17.3 J/cm^2 laser fluence.

a) **b)**

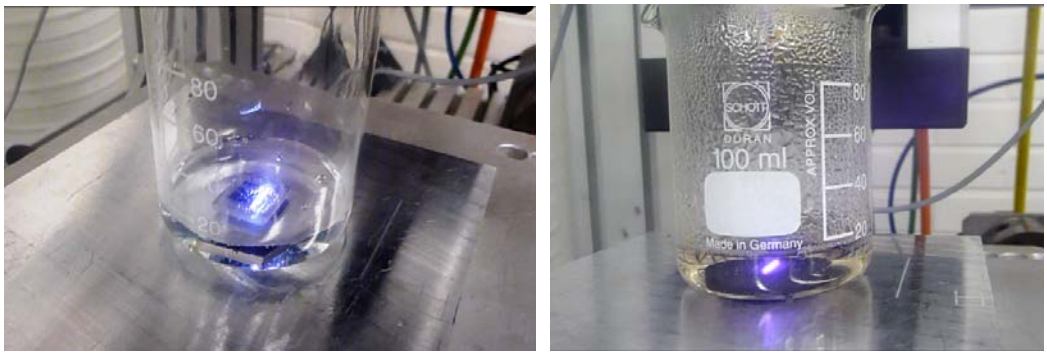

Figure 4.1 *Pulsed laser ablation of Titanium* ***a)*** *and Graphite* ***b)*** *in action and the bright plasma is visible in each case just above the target.*

During the ablation, the liquid heated up and evaporated which is visible in figure 4.1b. Due to this, the liquid level above the target changed and had to be kept constant by consistently topping it up to the marked level.

4.1.1 Pulsed laser ablation of Titanium in Deionised water

Pure titanium targets were ablated in deionised water at the laser powers 12%, 15%, 18%, 20%, 30%, 40%, 50 and 60% of the maximum power. The synthesised suspensions were blue in colour which is characteristic of TiO_2 nanoparticles and the colour of suspension became more intense on increasing the duration of ablation and also on increasing the power. But after a certain value of laser power, the colour of suspension started to become less intense. The formation of nanoparticles has been explained in the theoretical background of this thesis. The figure 4.2 shows the suspensions prepared with laser powers 12%, 20%, 30%, 40% and 50%, four hours after the pulsed laser ablation process. This can be compared with figure 4.3 which shows the suspensions 100 hours after the ablation process.

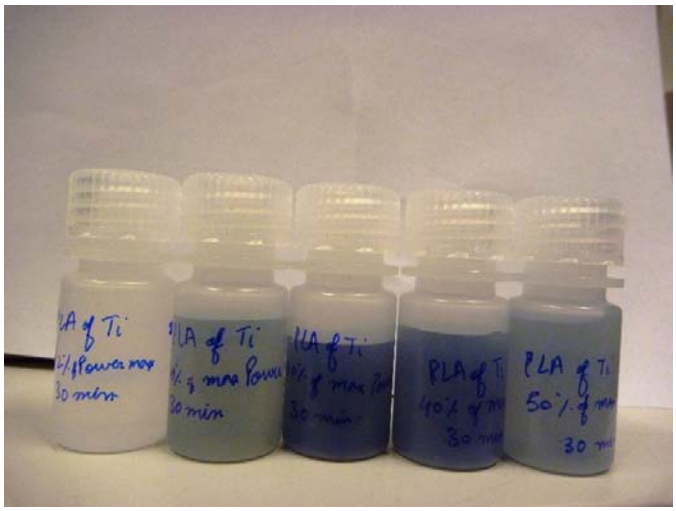

Figure 4.2 *TiO_2 suspensions 4 hours after ablation. From left to right the suspensions have been prepared at laser powers 12%, 20%, 30%, 40% and 50%. All the suspensions have a characteristic blue colour. The intensity of the colour varies with the concentration of nanoparticles in it.*

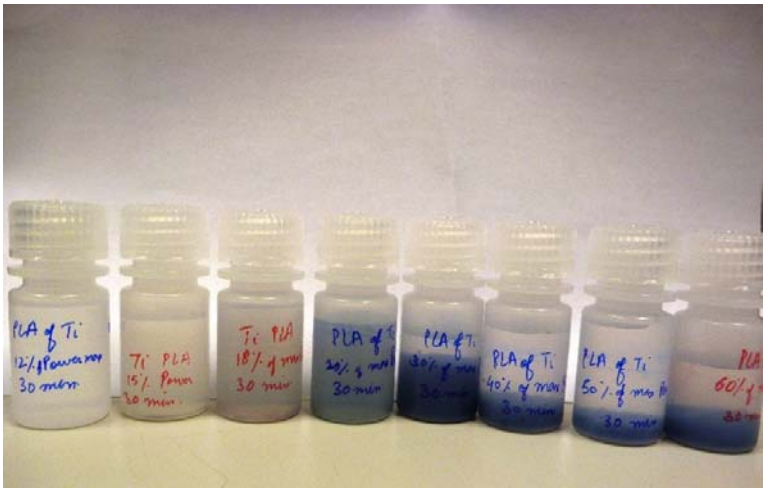

Figure 4.3 *TiO_2 suspensions 100 hours after ablation. From left to right the suspensions have been prepared at laser powers 12%, 15%, 18%, 20%, 30%, 40%, 50 and 60%. Sedimentation after agglomeration is visible in suspensions synthesised at laser powers 30% and higher.*

Right after the ablation, the suspensions were well dispersed and even four hours later they were stable (figure 4.2). However, the suspensions formed sediments after 100 hours of ablation process (figure 4.3). In some suspensions, the sediments were in the form of gel.

4.1.2 Pulsed laser ablation of Graphite in Deionised water

Pure graphite targets were also ablated in deionised water and the laser powers used were 15%, 40%, 50%, 60%, 80% and 100% of the maximum laser power. The synthesised suspensions were grey in colour because of the ablated carbon nanoparticles. During and right after the ablation higher powers gave more intense colour but sedimentation in them caused the less intense colour as shown in figure 4.4 for suspensions which were obtained by ablation of graphite at laser powers 40%, 60%, 80% and 100% of the maximum power.

Figure 4.4 *The suspensions synthesised by pulsed laser ablation of graphite. From left to right the suspensions have been prepared at laser powers 40%, 60%, 80% and 100%. All the suspensions have a characteristic grey colour with darker agglomerates.*

As the laser power was increased, bigger particles and chunks from the target surface were ablated and they formed sediments right after the ablation process finished. During the ablation process, the particles were being stirred due to heavy bubbling and cavitation. Sedimentation happens partly because water does not wet the surface of carbon nanoparticles. Water is polar and carbon is non-polar substance. Due to this, the carbon nano particles agglomerate and form sediments at the base of the storage vessel.

4.1.3 Synthesis yield measurements and effect of laser power and laser fluence on the yield of nanoparticles

As seen in the last section, the laser power has a significant effect on the concentration of the suspensions. However, this effect is not completely straight forward. The increase in laser power does not necessarily increase the laser fluence because the spot diameter also changes. Due to this, spot size of crater diameter on the ablated target surface was measured for different values of laser power so that the exact laser fluence values could be determined. The spot size measurement for laser powers less than 40% of the maximum were not possible. Figure 4.5 and table 4-1 show the spot sizes measured for laser powers 40%, 60%, 80% and 100% of the maximum power. The minimum spot size was 50 µm which was already known for lower powers.

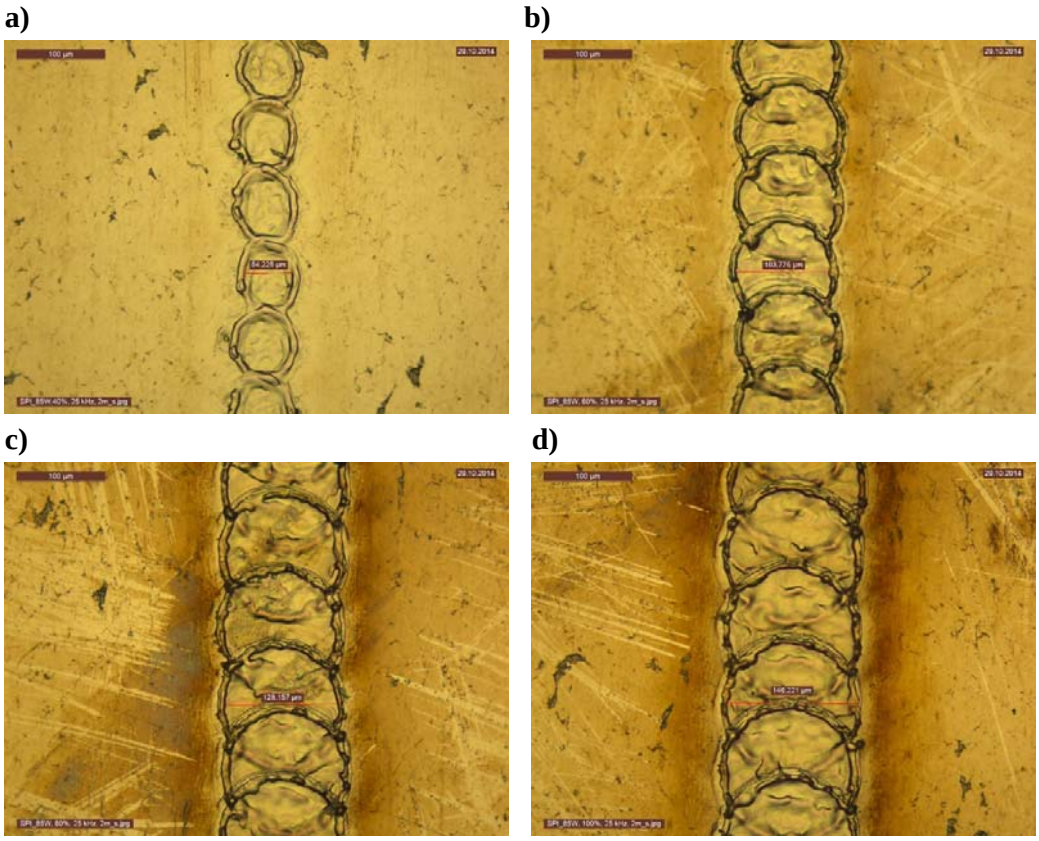

Figure 4.5 *The spot size measurements on a steel specimen are shown in the above micrographs for laser powers* ***a)*** *40%,* ***b)*** *60%,* ***c)*** *80%, and* ***d)*** *100% laser power. The measured spot sizes have been marked in the images.*

Table 4-1 *Spot size measurements at different laser powers*

S. No.	Percentage of max. laser power (85W)	Spot diameter (μm)
1	20%	50.00
2	40%	54.22
3	60%	103.77
4	80%	128.15
5	100%	146.22

Laser fluence [J/cm^2] is the energy per unit area that is available from a laser pulse. The maximum energy per pulse was known to be 3.4 mJ and also the spot size values corresponding to the laser power were measured as shown in table 4-1. Table 4-2 shows the laser fluence measurements that were calculated from measured spot diameter values.

Table 4-2 *Laser fluence measurements corresponding to the laser powers*

S. No.	Percentage of max. laser power (85W)	Laser Fluence [J/cm^2]
1	20%	34.65
2	40%	58.92
3	60%	24.13
4	80%	21.09
5	100%	20.26

The relation between the experimental laser fluence and laser power is shown in figure 4.6 .The laser fluence increases as the laser power increases until 40% power followed by a drop at 60% , 80% and 100% of the maximum laser power.

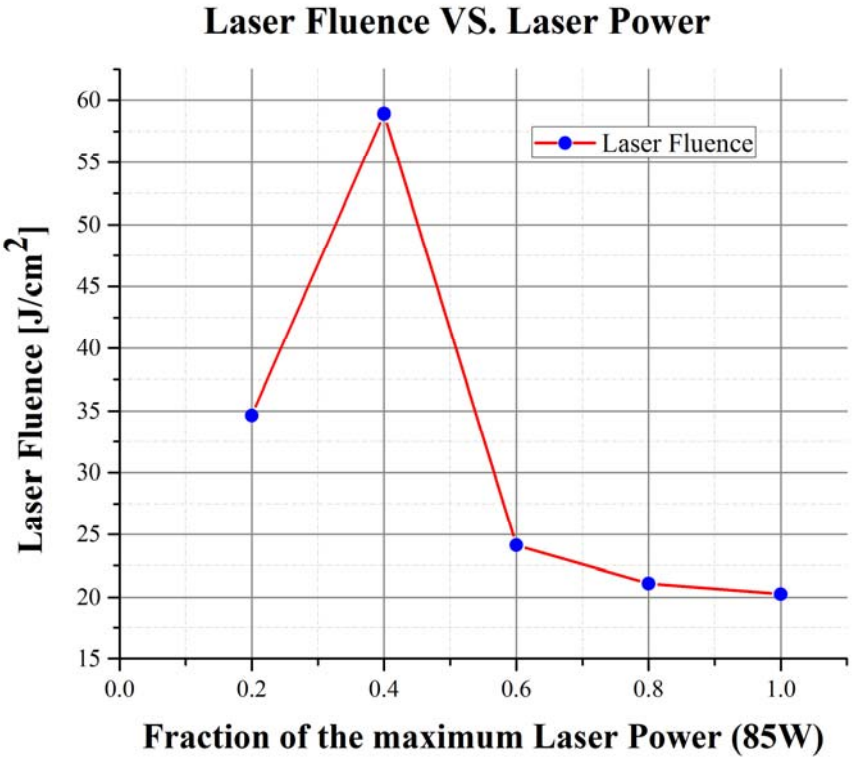

Figure 4.6 *The experimental trend between the laser fluence and the laser power*

The peak at 40% power in figure 4.6 means that the laser fluence or in simpler terms, the localised energy, is the highest at that point due to the optimum combination of spot size and laser power. On the other hand, the total energy that goes into the system with the laser beam increases as we increase the power of the laser until it reaches a maxima at 100% laser power which was 85 watts.

The effect of this varying laser fluence on the agglomeration and consequently on the sedimentation can be observed from figures 4.3 and 4.7 that were taken 100 hours and 170 hours after ablation respectively. The nanoparticles density and amount in the 12%, 15% and 18% laser power synthesised suspensions was very few which was why they

look the same 100 hours and 170 hours after ablation. The sedimentation in suspensions produced using 40%, 50 and 60% laser power was much faster compared to other suspensions. It is worthwhile mentioning that the suspension synthesised using 20% of the maximum laser power was stable even 170 hours after the ablation.

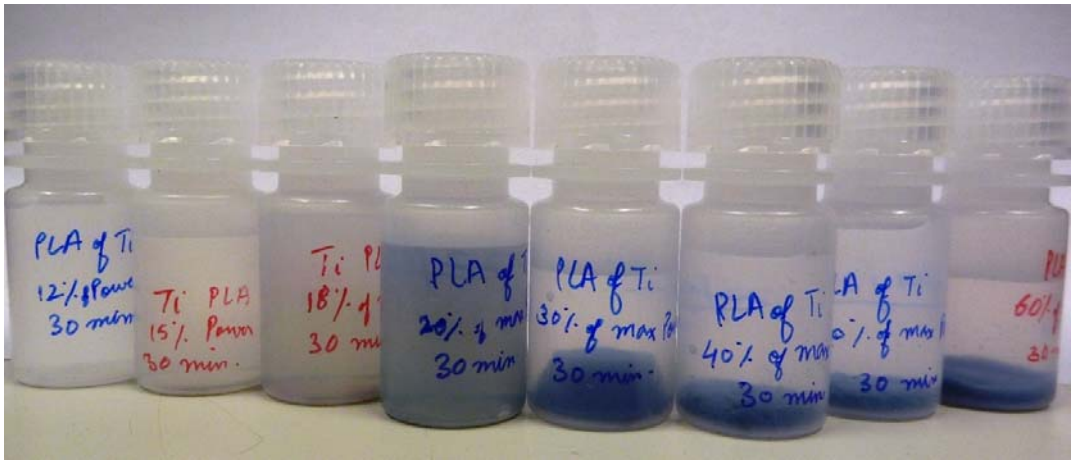

Figure 4.7 *TiO_2 suspensions 170 hours after ablation. From left to right the suspensions have been prepared at laser powers 12%, 15%, 18%, 20%, 30%, 40%, 50 and 60%. Sedimentation visible in suspensions made at 30%, 40%, 50% and 60% laser power. The suspension made with 20% laser power is still stable.*

Further analysis of these suspensions through mass measurements by drying them and weighing the nanoparticle powder resulted in a trend that is shown in figure 4.8. The increase in the yield of nanoparticles is noticeable until 40% laser power and thereafter the amount of nanoparticles produced is decreased. The trend in the yield of the nanoparticles can be explained with the increasing laser fluence until 40% and then decreases afterwards (figure 4.6). The sample weight corresponding to 50% power should be higher or the sample weight for 60% power should be lower in order to exactly follow the curve in figure 4.6. The amount of nanoparticles produced by pulsed laser ablation of titanium with 50% and 60% power for 30 minutes were 11.3 mg and 14.3 mg respectively. As the power increases the spot size also increases (as mentioned earlier in spot size measurements in this section) and due to that the overlap of spots is also more. This increase in overlap leads to accumulation of energy of several beams before the next pulse irradiates the same spot and gives rise to the decrease of the threshold laser fluence of the target material. This is proposed as the reason for greater amount of nanoparticles ablated from the titanium target at 60% as compared to 50% of the maximum laser power even though the laser fluence is decreasing.

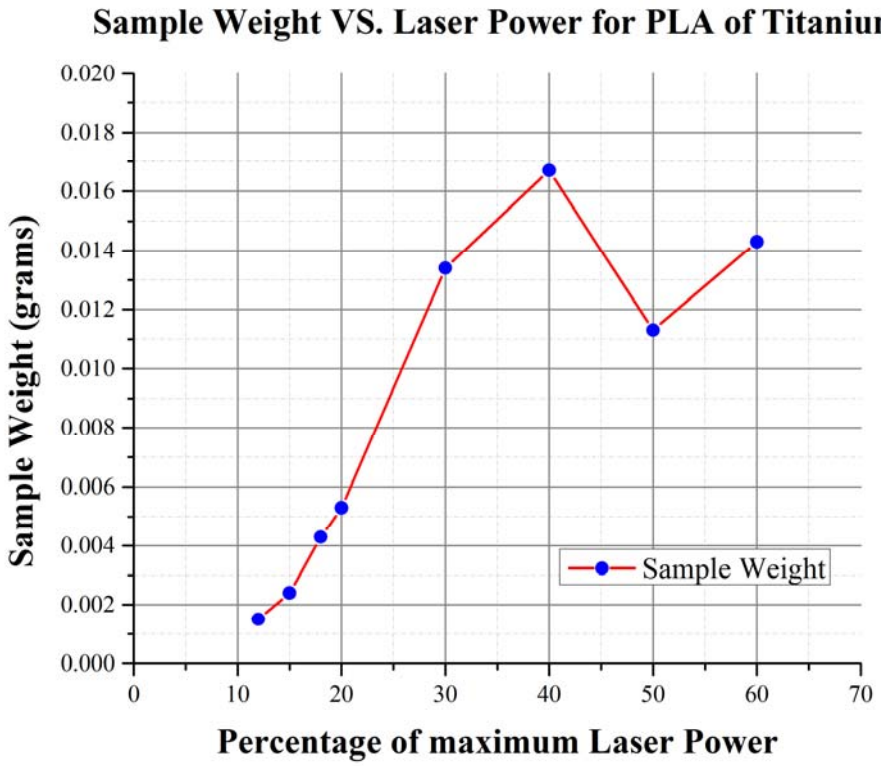

Figure 4.8 *The graph between the weight of TiO_2 nanoparticles produced and the laser power used shows an increasing trend until 40% power.*

From figure 4.8, it can be seen that the amount of nanoparticles produced at 30% laser power is less than that at 40% laser power. However, if we compare this result to figure 4.7, it can be seen that the sediment in suspension prepared by 30% laser power is much larger in volume to the sediment in 40% laser power suspension. This was analysed to be caused because the sediment in the former was gel like and further compaction was not possible. In the TEM section (4.2.1) of characterisation results, it has been mentioned that both crystalline as well as amorphous phases were present in the sample. This amorphous phase is present in the form of a network and acts as s skeleton that binds the nanoparticles together upon agglomeration. Due to this, the compaction under gravity is less and the sediment behaves like a gel. Therefore, the decrease in the volume of sediments from the 30% to 40% samples could be due to the decreased amount of the skeletal amorphous phase.

Similar weight measurements of the nanoparticles produced by pulsed laser ablation of graphite are shown in figure 4.9.

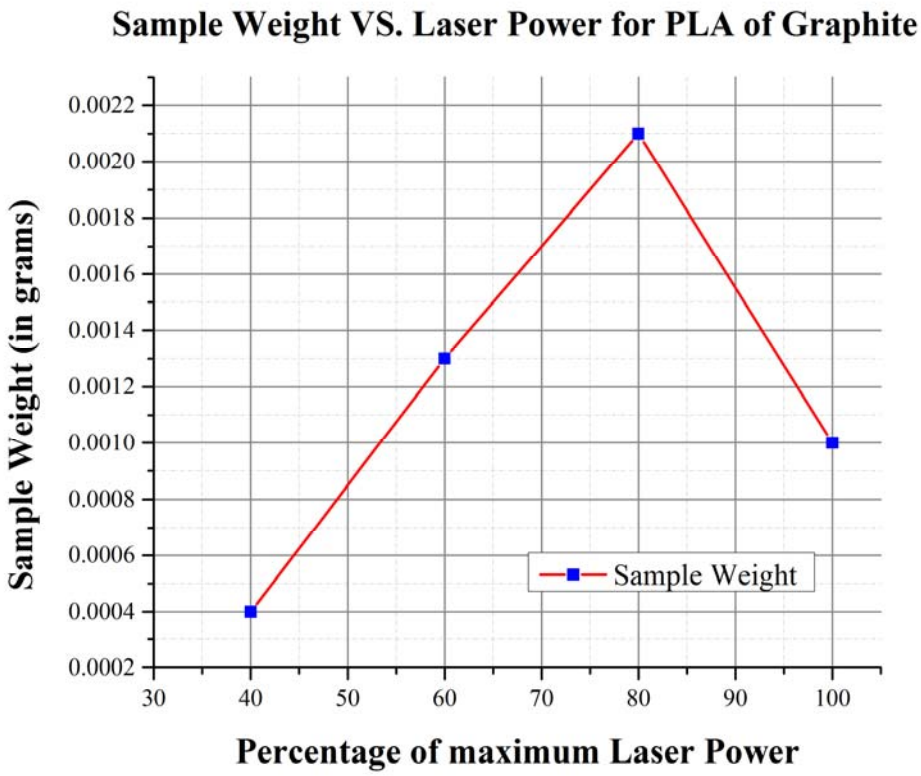

Figure 4.9 *The graph between the weight of carbon nanoparticles produced and the laser power used shows an increasing trend until 80% power.*

Figure 4.9 shows an increasing trend in the weight of nanoparticles produced from 40% power to 80% power and the relationship between the sample weights with the increasing power is linear. After that, at 100% power, decrease in the weight of nanoparticles was observed. These laser powers are much higher than the laser powers used for titanium targets and it is important to notice that at these higher powers the liquid also gets heated up and continuous evaporation was observed when 100% laser power was used. The steam so formed upon evaporation interacts with the laser and may vary the focussing of the laser beam so that the laser beam is no longer focussed on the target surface. This is proposed to lead to decreased laser fluence and subsequently lower yield of nanoparticles produced. The graphite target requires much higher laser powers as compared to titanium for ablation. The increase in the laser power is proportional to the increase in the yield of nanoparticles until solvent effects such as evaporation come into play. This also means that the yield of nanoparticles in graphite does not follow the laser fluence curve.

4.2 Characterisation results for nanoparticles and targets

In this section, the characterisation results from the transmission electron microscopy, small angle x-ray scattering, x-ray diffraction and wide angle x-ray scattering are discussed for nanoparticle suspensions synthesised from titanium and graphite. Furthermore, the results from characterisation of pulsed laser ablated titanium and graphite targets by x-ray diffraction and optical profilometry are presented and discussed.

4.2.1 Transmission electron microscopy of nanoparticles

Both for pure titanium and pure graphite, some initial pulsed laser ablation tests were carried out. They were followed by a series of tests for both samples. In this sub-section, the TEM results for suspensions obtained from ablation of titanium are stated and followed by TEM results for suspensions obtained from ablation of graphite.

4.2.1.1 Transmission electron microscopy of nanoparticle suspensions ablated from titanium

The initial pulsed laser ablation test on titanium target was performed using 20% of the maximum laser power and for short ablation duration of 10 minutes to test the experimental ablation setup and analyse the particle size and shape. Further, to understand the effect of laser fluence and laser power on the particle size, shape and size distribution, a series of pulsed laser ablation tests were performed on titanium target. These tests included pulsed laser ablation of titanium with laser powers 15%, 18%, 20%, 30% 40%, 50%, and 60% of the maximum laser power for a duration of 30 minutes in each experiment. The variation in the laser fluency was not proportional to the variation in the laser power, since the spot diameter was also varying without any uniformity.

Figure 4.10 shows the transmission electron microscope images of the nanoparticle suspension synthesised at 20% of the maximum laser power for 10 minutes ablation. Figure 4.10a, 4.10b, and 4.10c show nanoparticles with different magnifications taken from the same location as marked in 4.10a. Some of the nanoparticles were perfectly round as can be seen in the higher magnification image in figure 4.10c. In these images, the particle size of nanoparticles varied between 4 nm and 30 nm. Figure 4.10d shows the electron diffraction pattern taken from the same spot as the images in figure 4.10c. The round shaped nanoparticles were crystalline and this was observed from the electron diffraction pattern of this sample and from phase contrast in TEM. These round shaped nanoparticles were surrounded by a network of amorphous phase which was also titanium based oxide.

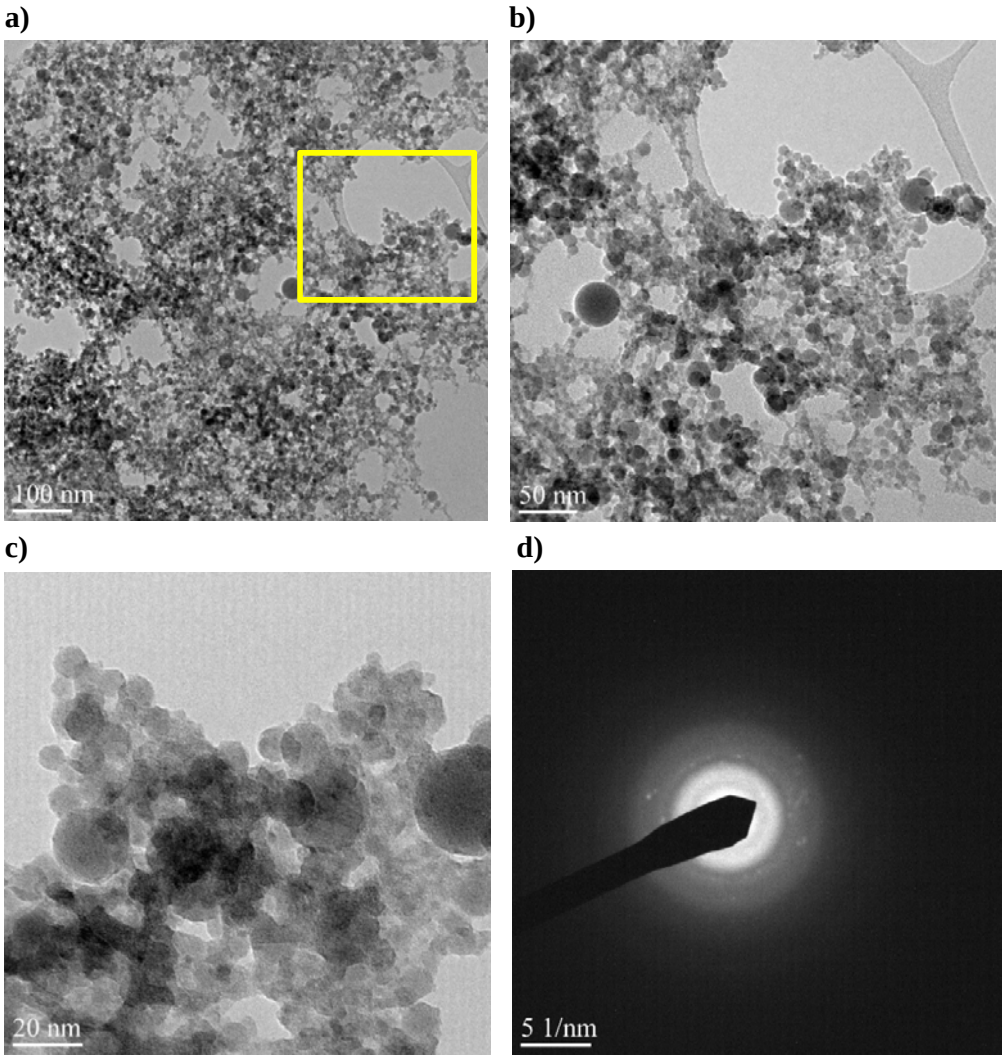

Figure 4.10 *TEM images **a)**, **b)**, and **c)** showing round nanoparticles. The particles were perfectly round. In **c)** The nanoparticles smaller than 5 nm were observed in the TEM of the sample. Some of those can be seen in the top left corner of the image. **d)** The synthesised nanoparticles were crystalline. The bright spots in the diffraction pattern represent the crystalline phase present in the sample. The spots became brighter when the size of particles increased.*

This initial experiment aroused the interest to study the effect of different laser powers and different laser fluencies on the shape, size and size distribution of the nanoparticles. So after this initial test, a series of pulsed laser ablation tests on titanium with different laser powers and laser fluencies each time were performed. The tests included pulsed laser ablation of titanium with laser powers 15%, 18%, 20%, 30%, 40%, 50%, and 60% of the maximum laser power for a duration of 30 minutes in each experiment.

Figures 4.11 - 4.17 represent the TEM images of the suspensions synthesised at laser powers 15%, 18%, 20%, 30%, 40%, 50%, and 60% respectively.

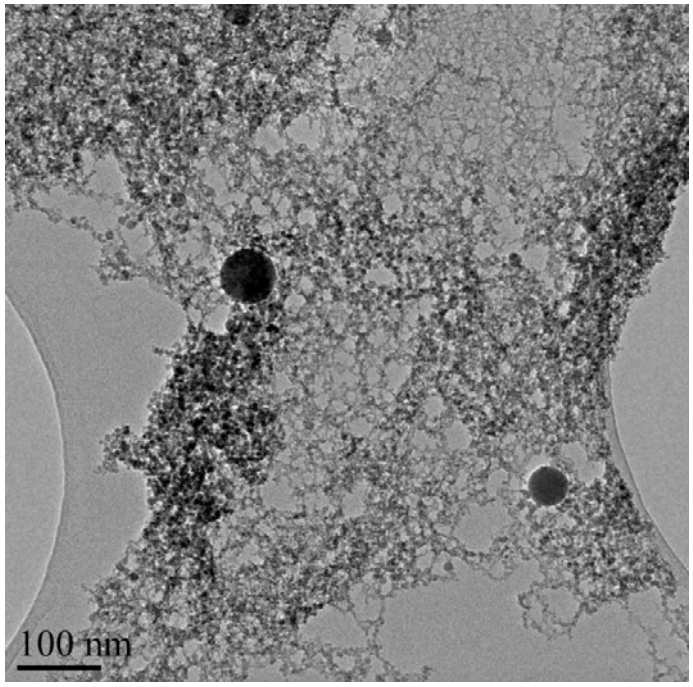

Figure 4.11 *TEM image (15% laser power, 30 minutes) shows two bigger nanoparticles about 32 and 63 nm in size as compared to the much smaller nanoparticles (4-12 nm) that can be seen in the dark and dense region just below the bigger particle.*

In figure 4.11 the particle size range was 4-12 nm for smaller nanoparticles and there were also two bigger nanoparticles present with sizes approximately 32 nm and 63 nm. In figure 4.12, several nanoparticles in the particle size range 5-15 nm in diameter were observed. The TEM image in figure 4.13 represents the suspension synthesised at laser power 20% and particles with a very narrow size distribution are noticeable in the image. In figures 4.14, 4.15, 4.16, and 4.17, there were some regions in each image that were heavily agglomerated.

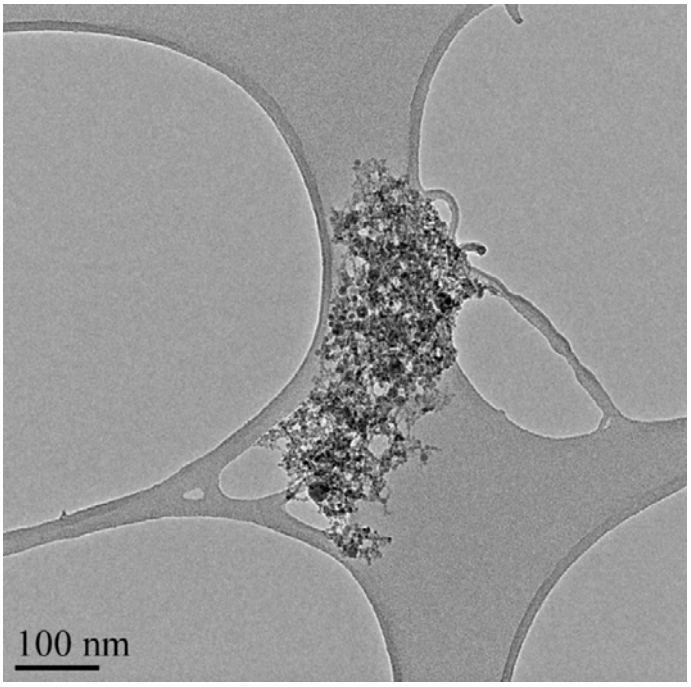

Figure 4.12 *Some nanoparticles are visible in the TEM image (18% laser power, 30 minutes). The size of these particles ranges between 5 nm and 15 nm. They are surrounded by a network of amorphous phase.*

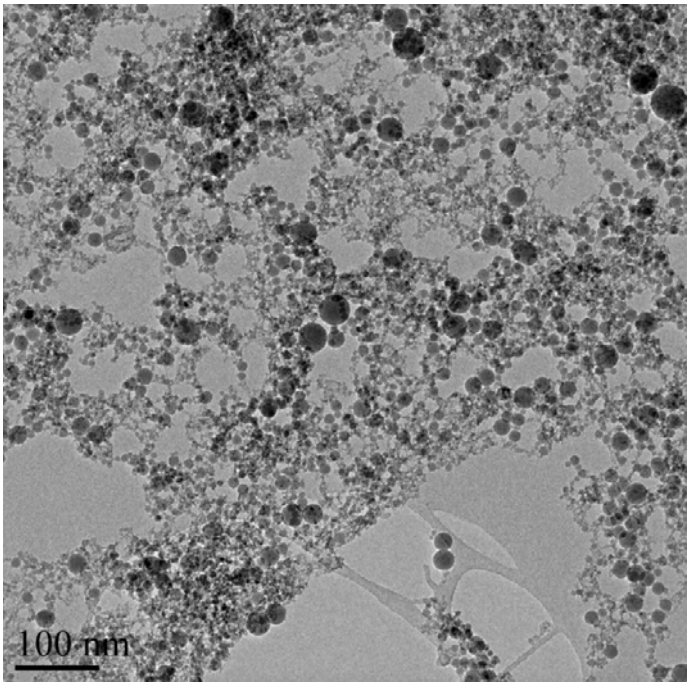

Figure 4.13 *TEM image shows round TiO_2 particles with different sizes in suspension synthesised at 20% laser power and 30 minutes ablation time.*

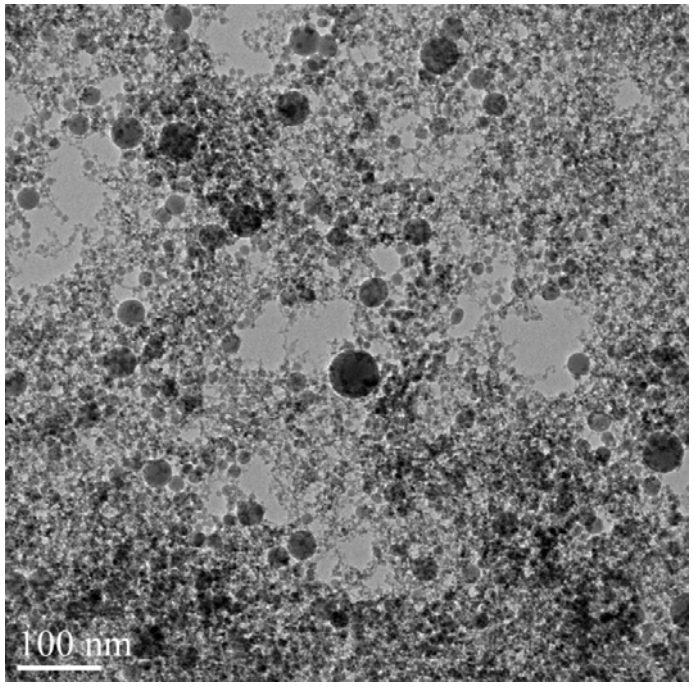

Figure 4.14 *In this TEM image (30% laser power, 30 minutes), the nanoparticle concentration is higher than in suspension made at 20% of the maximum laser power.*

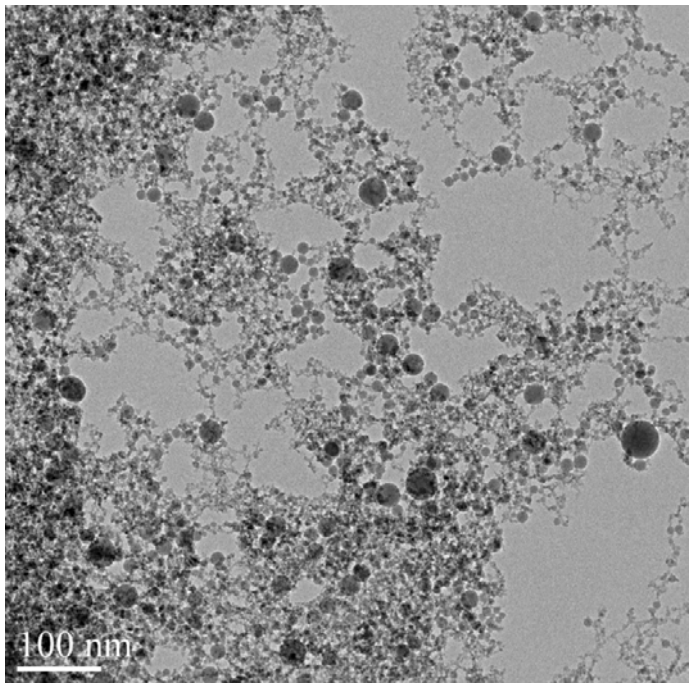

Figure 4.15 *TEM image (40% laser power, 30 minutes) shows nanoparticles produced at 40% laser power. The nanoparticle concentration is less than in suspension made at 30% laser power.*

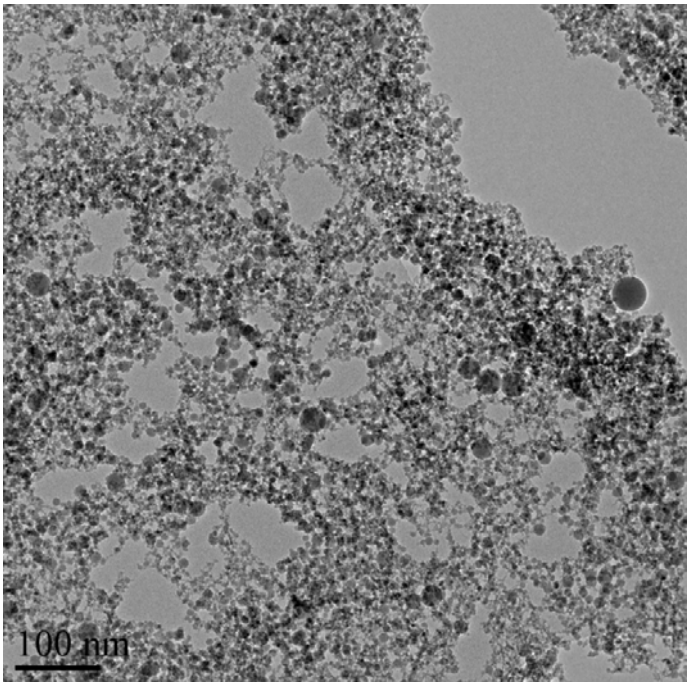

Figure 4.16 *TEM image (50% laser power, 30 minutes) shows nanoparticles with a narrow size distribution. Only few large nanoparticles are visible in the TEM view of the sample.*

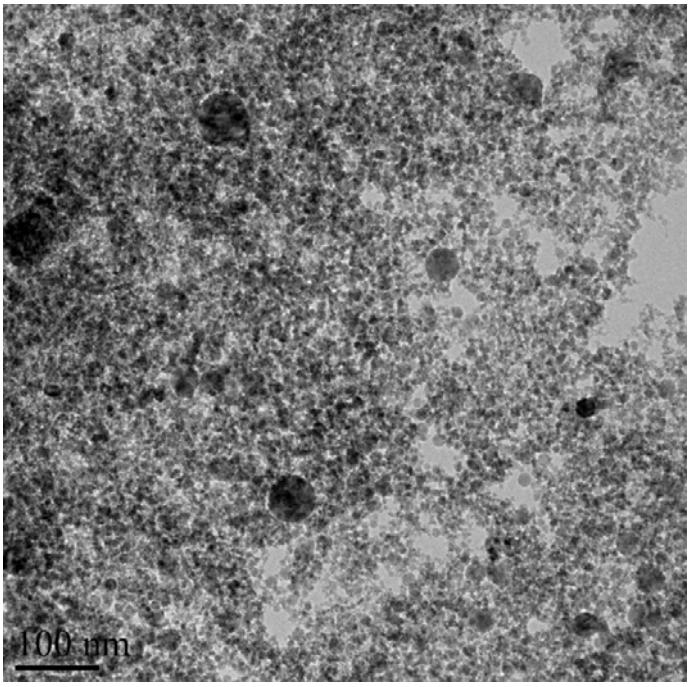

Figure 4.17 *TEM image (60% laser power, 30 minutes) shows highly concentrated nanoparticles. The dark regions show that there are multiple nanoparticles on top of each other.*

With all the different laser power values, the shape of the nanoparticles remains round. This is because the when the atoms and ionised species incorporate to form nanoparticles,

the sphere is the shape with the least surface energy. So, in order to decrease the surface energy and also the total energy, the particles formed are round. From the figures 4.11 – 4.17, it can also be observed that the average particle size appears to be almost the same but there seems to be varying number of the larger nanoparticles and there is already noticeable size distribution. For this, size distribution was measured by manually calculating the particle size from TEM images and later also by small angle x-ray scattering of the nanoparticle suspensions. The size distribution results from both techniques are presented later in this chapter.

The amount of amorphous phase present in the sample prepared at different laser powers changed. According to the earlier results from sedimentation, we deduced that the amount of the skeletal amorphous phase decreases from 30% to 40% laser power and therefore, the volume of the sediment decreases. The TEM images cannot be used to validate this since the amount of amorphous phase is difficult to measure.

The crystallinity of the round shaped nanoparticles were confirmed from the electron diffraction patterns of the corresponding samples. The larger round shaped nanoparticles resulted in larger bright spots in the electron diffraction pattern. The diffraction pattern also showed halo which is characteristic of amorphous phase since the x-ray get scattered more. From the TEM images, phase contrast was observed which confirms the crystallinity of the round nanoparticles but at very high magnification the quality of the TEM images was not god enough to resolve phase contrast for each sample.

4.2.1.2 Transmission electron microscopy of carbon nanoparticles

Similar to pulsed laser ablation of titanium, initial tests were also performed on graphite targets using 15% and 50% of maximum laser power and 20 minutes ablation time. Figures 4.18 – 4.20 show the corresponding TEM results from these initial tests.

For the suspensions synthesised at 15 % laser power, the TEM results showed carbon nanotubes in the samples at 400,000 x magnification (Figure 4.18 and 4.20). In figure 4.18, the region containing carbon nanotubes has been marked. The scale bar is 5 nanometres. The electron diffraction pattern (figure 4.19) from the same region as in the figure 4.20 showed presence of nanocrystalline phase (distinct rings in the electron diffraction pattern) as well as amorphous phase (halo observed in the electron diffraction pattern) in the sample.

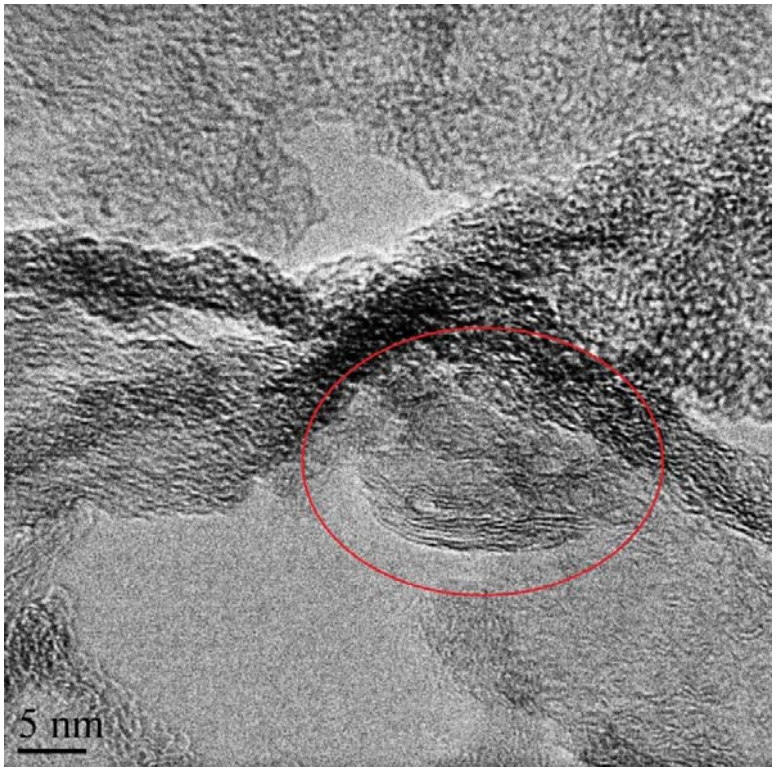

Figure 4.18 *TEM image shows carbon nanotubes in the carbon nanoparticle suspension synthesised at 15% laser power and for 20 minutes ablation time.*

Figure 4.19 *The electron diffraction pattern for the region in figure 4.21 shows nano-crystalline materials are present in the sample along with amorphous phase.*

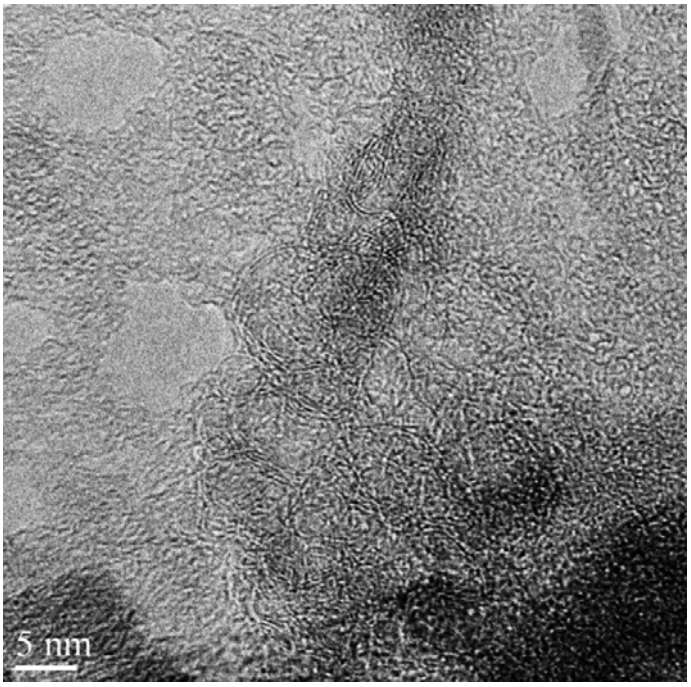

Figure 4.20 *TEM image of carbon nano particles produced at 50% laser power and 20 minutes ablation time.*

The distinctive feature of the carbon nanotubes synthesised is that they are multi-walled. So, there are a lot of folded few atom layer carbon nanoparticles. These features are visible in both figures 4.18 and 4.20.

The initial tests were immediately followed by a series of pulsed laser ablation tests with powers 40%, 60%, 80%, and 100% of the maximum laser power and ablation time of 30 minutes for each test. Figures 4.21a-d show the TEM results for these tests. For each value of laser power, carbon nanotubes could be observed in the TEM images. The TEM images at higher magnifications were not of good quality, so the phase contrast could not be detected. Due to this, the effect of laser power could not be established in these samples.

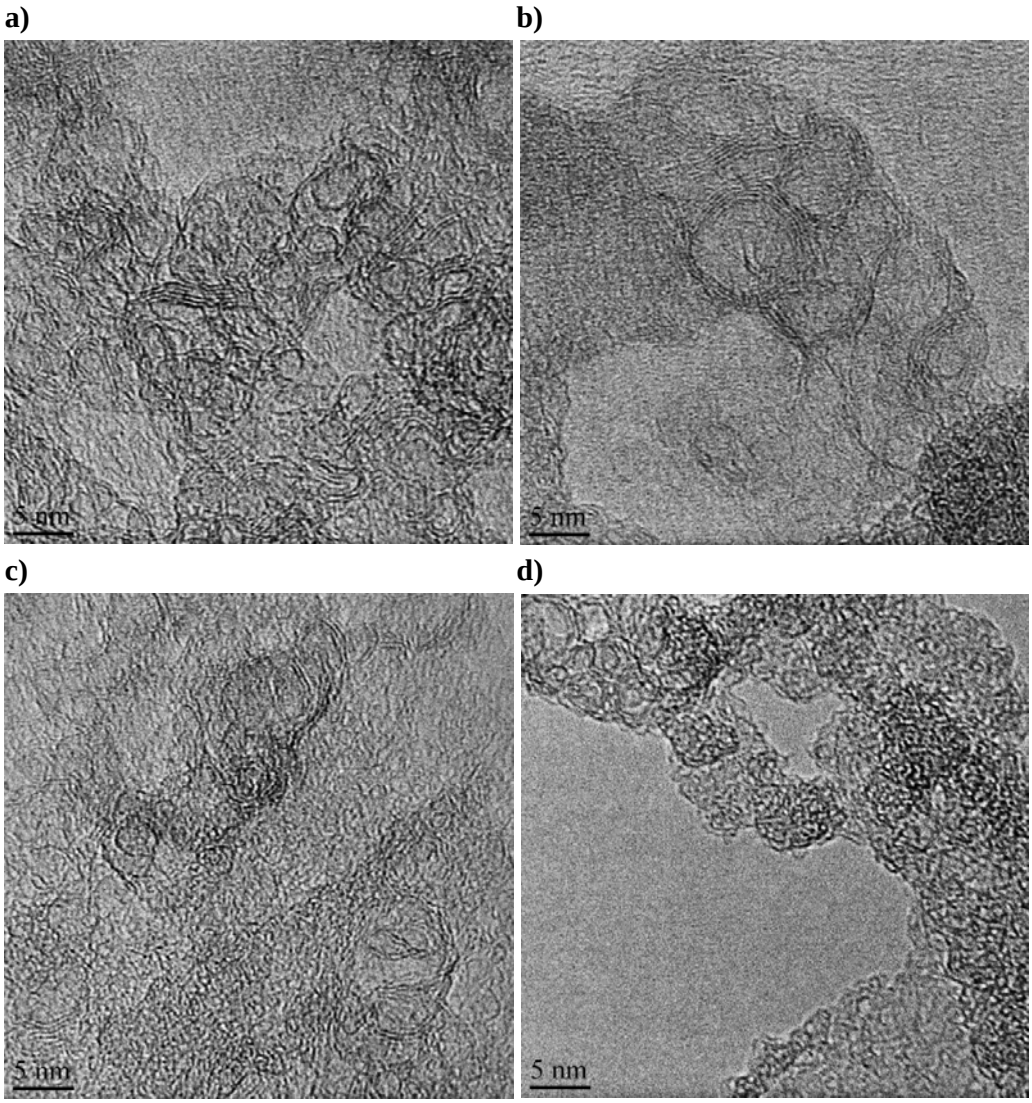

Figure 4.21 *TEM images* ***a)***, ***b)***, ***c)*** *and* ***d)*** *show carbon nanotubes surrounded by amorphous phase carbon nanomaterials. The number of walls for a particular carbon nanotube varies in each image.*

The formation of carbon nanotubes can be explained by the theory proposed by Al-Hamaoy et al [16]. Carbon nanotubes were formed because of the high repetition rate used with the laser due to which the laser fluence per unit time was high. This resulted in generation of very high pressures and temperatures upon the collapse of the bubbles. At this high temperature and pressure, novel materials such as carbon nanotubes are produced.

4.2.1.3 Energy Dispersive Spectroscopy of nanoparticles

For characterisation of the elements present in the TEM samples of suspensions obtained by pulsed laser ablated titanium and graphite, energy dispersive spectroscopic measurements were performed. Figure 4.22 shows the TEM image of suspension ablated from

titanium. It shows the region of the sample where the EDS measurements were performed. The EDS results for one titanium and one graphite sample of the several samples that were examined using TEM are presented in figures 4.23, 4.24, and 4.25.

For titanium, TEM sample made from the suspension that was synthesised at 18% laser power and ablation time 30 minutes was used for EDS analysis. The measurements showed titanium and oxygen peaks in the EDS spectra (figures 4.23 and 4.24). Other significant peaks present in the EDS pattern belonged to carbon and copper. These elements were not present in the sample but they are from the copper grid which has a carbon layer on it. Small peaks of phosphorus, calcium, potassium, and silicon were also detected in the EDS 1 but not in EDS 2.

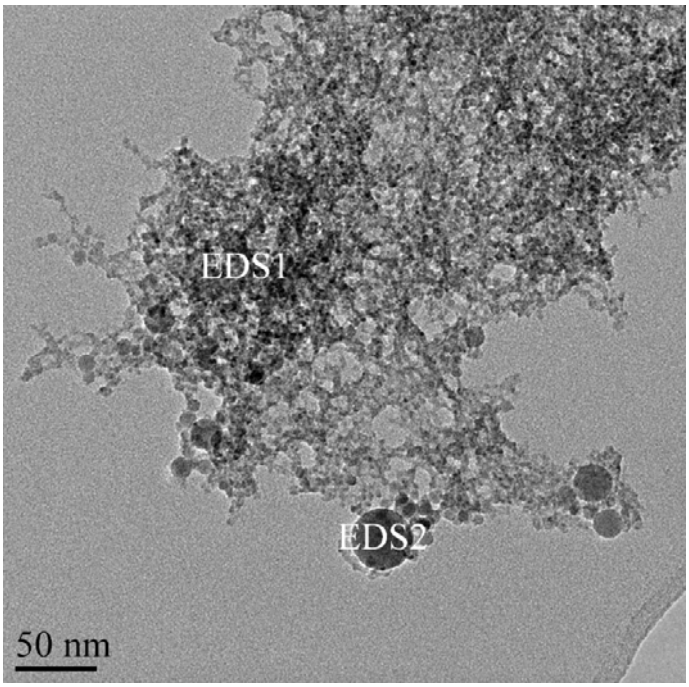

Figure 4.22 *TEM image showing the locations where EDS analysis was done. The titanium peak in EDS 1 was much higher than in EDS 2.*

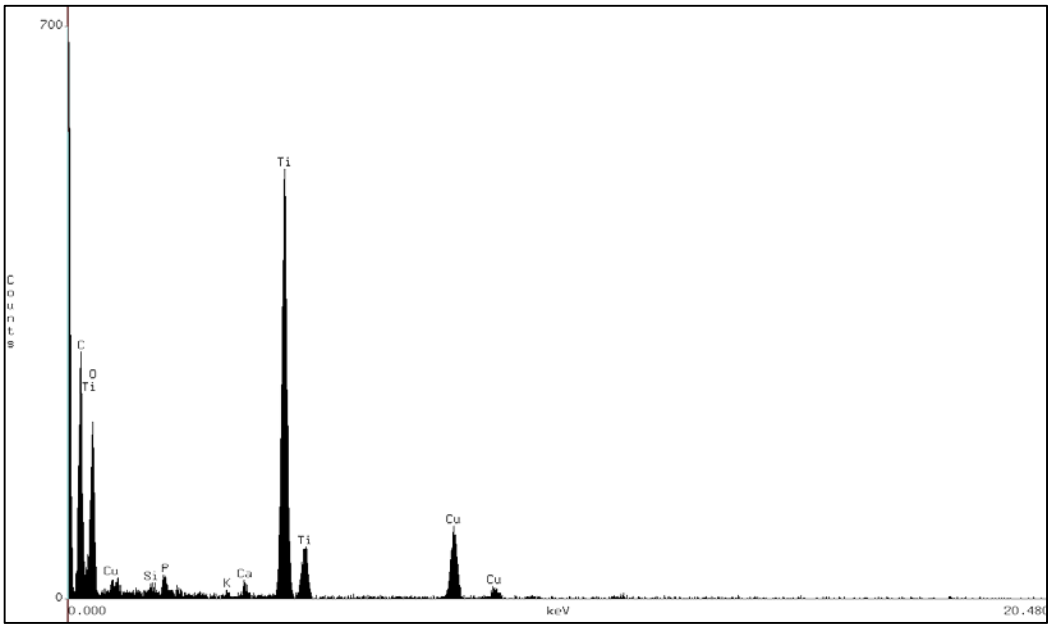

Figure 4.23 *This is EDS 1 spectra. Titanium and oxygen peaks are visible in the EDS pattern of pulsed laser ablated titanium sample with 18% laser power 30 minutes performed on the TEM sample. Other peaks belong to C, Cu, P, Ca, K, and Si.*

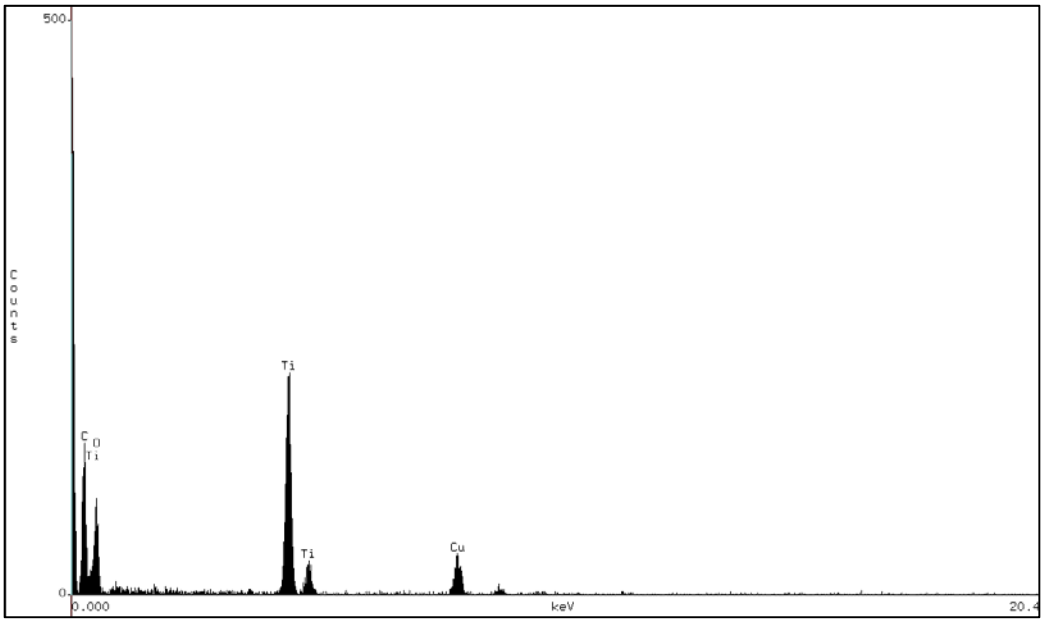

Figure 4.24 *This is the EDS 2 spectra. The titanium peak is visible but relatively shorter in the EDS pattern of pulsed laser ablated titanium sample with 18% laser power 30 minutes performed on the TEM sample. The oxygen peak is also present along with peaks for carbon and copper.*

The EDS analysis of pulsed laser ablated graphite sample with 50% laser power and 30 minutes ablation time is shown in the figure 4.25. Carbon peak is present in the EDS pattern. Other peak present is the copper peak. This peak is present in all the EDS patterns and comes from the TEM sample copper grid.

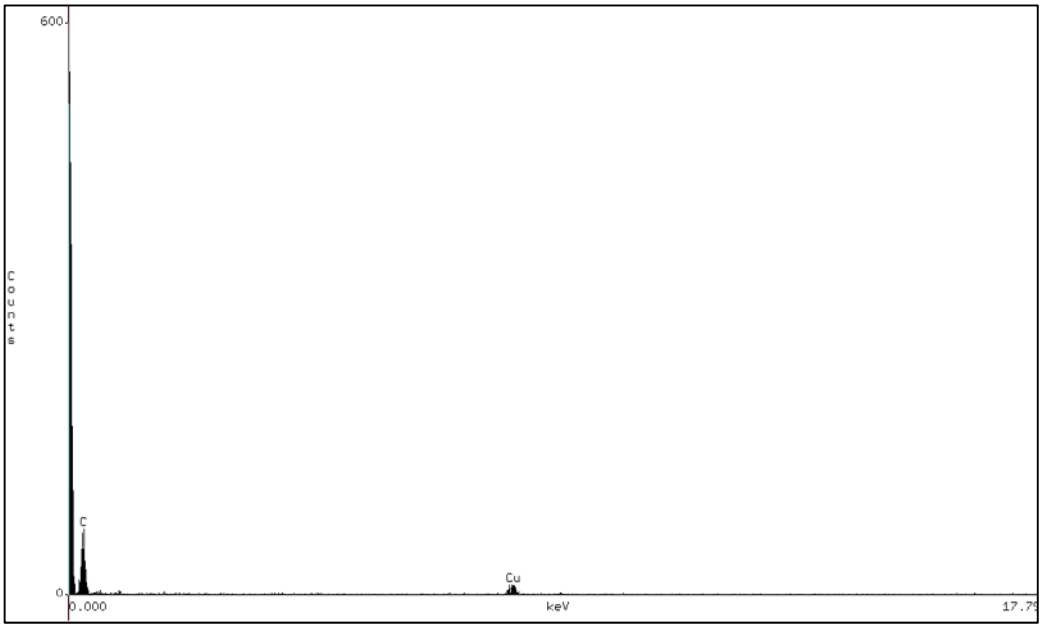

Figure 4.25 *Carbon peak is visible in the EDS pattern of pulsed laser ablated graphite sample with 50% laser power and 30 minutes ablation time performed on the TEM sample. The small copper peak comes from the copper grid of the TEM sample.*

These EDS measurements confirm the presence of titanium and oxygen in the suspensions formed by pulsed laser ablation of titanium. Similarly, in suspensions synthesised from graphite, the EDS results show nothing but carbon peak. Therefore, at this stage we know the elements present in the samples. For further analysis, to know the exact compounds or phases, x-ray diffraction was performed.

4.2.2 X-ray diffraction studies on the ablated targets and the synthesized powders

The x-ray diffraction measurements of the laser ablated targets and the synthesised powders were analysed using PANalytical data viewer and PANalytical highscore plus software. Figure 4.26 shows the x-ray diffraction pattern of the pulsed laser ablated graphite target. In this XRD pattern, diamond peak was observed. The location of the peak was at 43.9º. It is worthwhile mentioning that if the amount is detectable by XRD, then it means that diamond is present in relatively lasrge quantity on the surface of the graphite target. This indicates that the pulsed laser ablation of graphite in deionised water with laser fluence between 20 J/cm^2 and 60 J/cm^2 can produce diamond on the target surface.

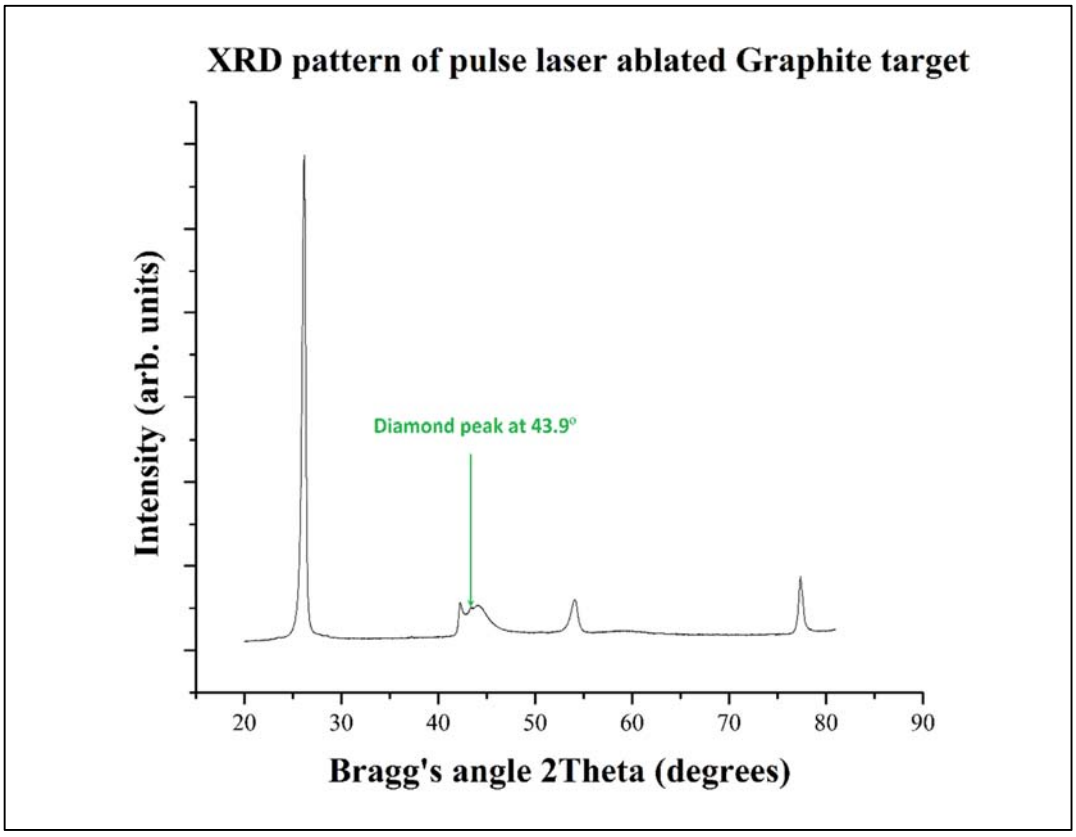

Figure 4.26 *Diamond peak at 43.9º visible in the X-ray Diffraction pattern of pulsed laser ablated graphite target*

The other peaks in the XRD pattern in figure 4.26 belonged to graphite. The target was pure graphite disc. The formation of novel material structures such as diamond could be due to the high repetition rate of the pulsed laser used. Al-Hamaoy et al. [16] reported the use of high frequency during the synthesis as the major reason for formation of novel material structures. Due to this higher frequency, the energy density per unit time was more and the collapsing bubbles gave rise to very high temperatures and pressures. The maximum repetition rate used by these authors was 14 kHz whereas in this thesis study, the repetition rate used was 25 kHz. So, the effect is even more intense than reported by Al-Hamaoy et al [16].

Figure 4.27 shows the XRD pattern of the pulsed laser ablated titanium target. In this XRD pattern, numerous peaks were detected. The major peaks were characteristic of titanium metal, anatase, rutile, titanium monoxide and titanium (III) oxide.

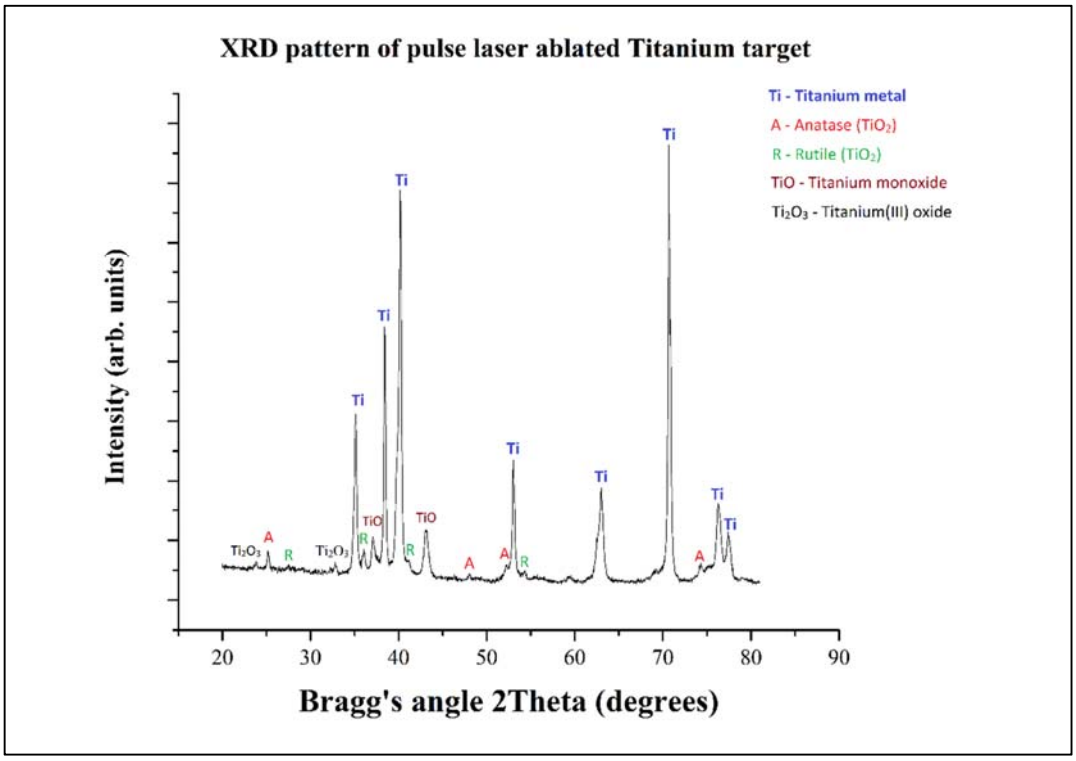

Figure 4.27 *Peaks for Titanium, Anatase, Brookite, Rutile, Titanium monoxide and Titanium (III) oxide are marked in the X-ray Diffraction pattern of pulsed laser ablated titanium target.*

Anatase and rutile are both polymorphs of titanium dioxide but their crystal structure is different and their energy band gap is also different. So, besides titanium metal, all three major types of oxides of titanium were present on the laser irradiated titanium target. The peaks for titanium had higher intensities compared to the oxides of titanium as can be seen in figure 4.27.

This measurement was followed by x-ray diffraction analysis of nanoparticle powder obtained after drying the suspensions. As shown in figure 4.28, there are numerous peaks in the XRD pattern for rutile and anatase. The suspension that was dried to produce nanoparticle powder for this measurement was synthesised by pulsed laser ablation of titanium at 30% laser power for 30 minutes.

In order to further analyse this nanoparticle powder, wide angle x-ray scattering was used. Figure 4.29 shows the wide angle x-ray scattering results for it. The WAXS results indicated the presence of not just anatase and rutile in the powder but also brookite. Brookite is also a polymorph of TiO_2 and its synthesis is the most difficult amongst other polymorphs anatase and rutile [25]. The mechanism of the particle formation in pulsed laser ablation is discussed in the theoretical background of this thesis. It is due to a narrow thermodynamic window available when the ablated species are in plasma that they form meta-stable phases. After sudden quenching of the plasma, the meta-stable species freeze out in the liquid [12]. In this case, these phases were anatase and brookite. This might be a reason why brookite, whose synthesis is challenging, was formed in this experiment.

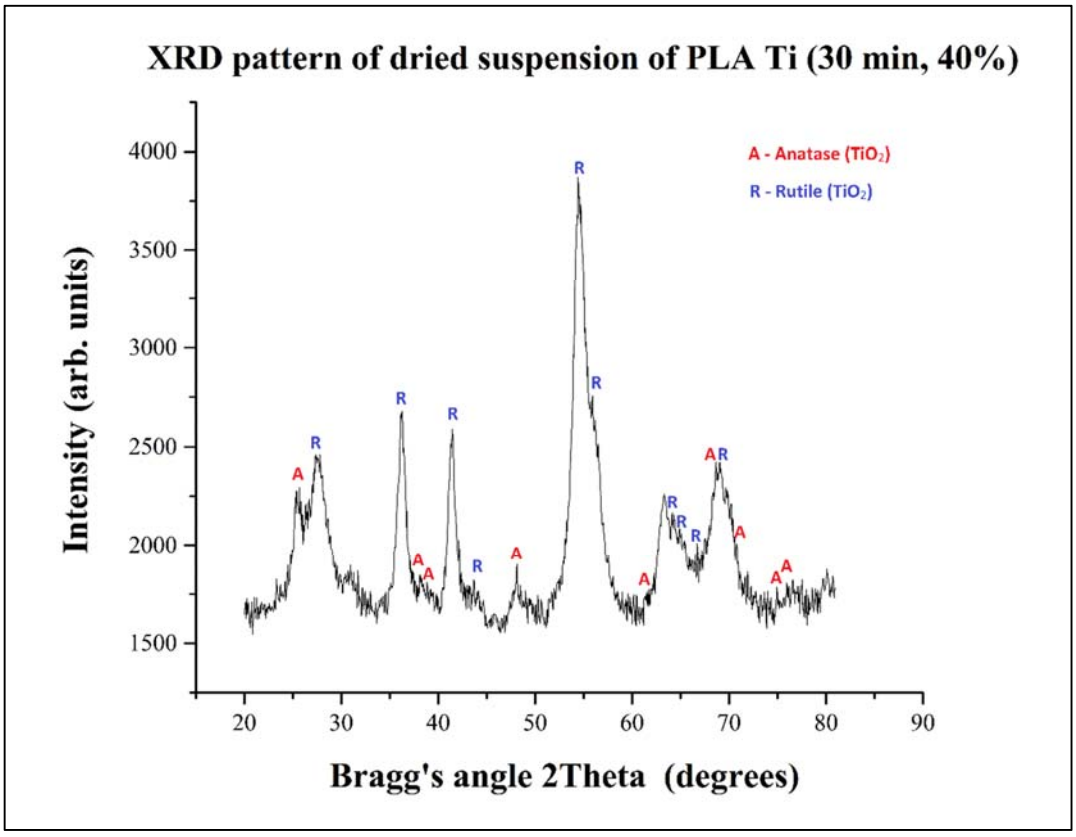

Figure 4.28 *Peaks for Anatase and Rutile are marked in the X-ray Diffraction pattern of TiO_2 nanoparticle powder obtained after drying the suspension.*

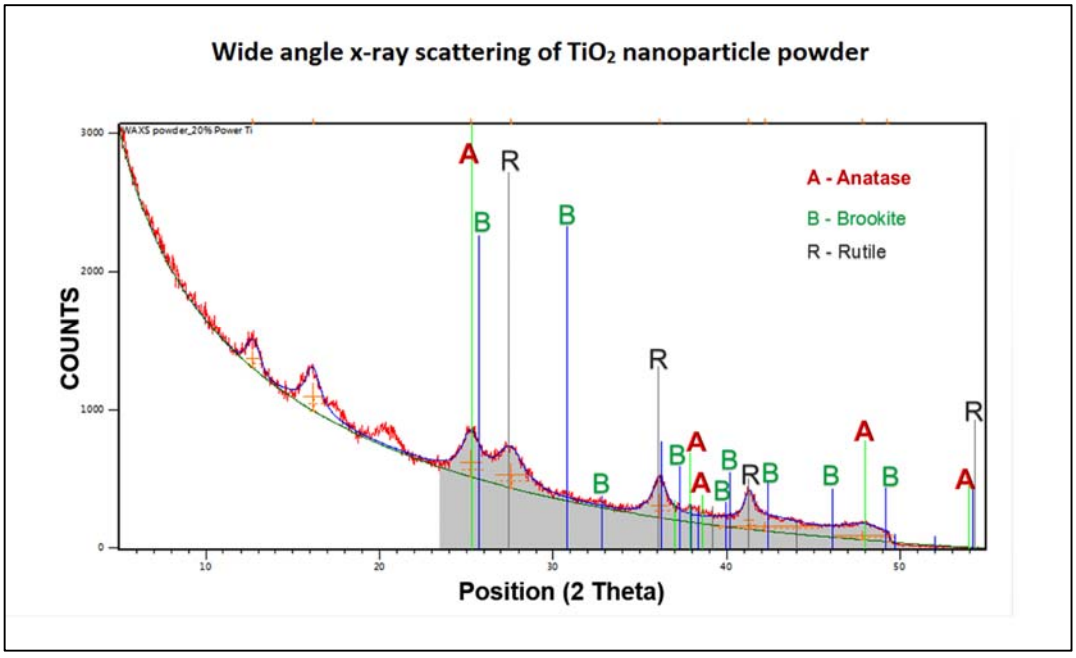

Figure 4.29 *Peaks for Anatase, Brookite and Rutile are marked in the wide angle x-ray scattering pattern of TiO_2 nanoparticle powder obtained after drying the suspension.*

In figure 4.29 it is important to notice that some peaks of brookite overlap with anatase and rutile peaks due to which its detection is also challenging.

XRD and WAXS results have confirmed that the nanoparticles produced in the pulsed laser ablation of titanium are different polymorphs of TiO_2. The quantity of PLA synthesized carbon nanopowders was not sufficient for XRD. So, XRD and WAXS measurements could not be performed for those samples.

4.2.3 Particle size distribution of the TiO_2 nanoparticles with TEM and SAXS

For the suspensions prepared by pulsed laser ablation of titanium, the particle size distributions were calculated by manually measuring the particle diameters from transmission electron microscope images to form a histogram showing the size distribution. Additionally the particle size distributions were also measured by small angle x-ray scattering (SAXS). The results from SAXS measurements were compared with the measurements from TEM images. From TEM images, diameters of 100 particles were measured to form histogram in each case.

Figures 4.30 and 4.31 represent the TEM image and the corresponding size distribution histogram from TEM image for suspension synthesised at 20% laser power and 20 minutes ablation respectively. These results are compared with the size distribution of nanoparticles determined by small angle x-ray scattering which is shown in figure 4.32. In figure 4.32, only the blue line, which is the cumulative undersize line, is of concern in this study.

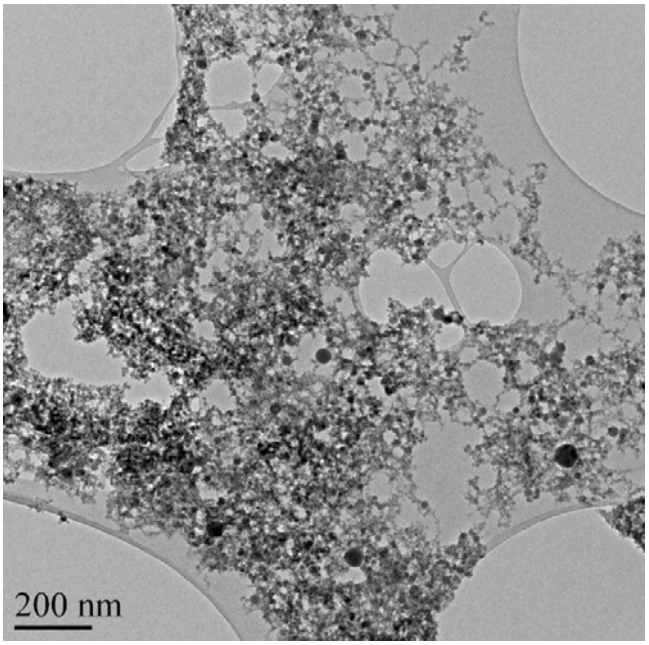

Figure 4.30 *TEM image from 20%, 20 minutes sample which was used to manually measure the particle sizes and form the corresponding histogram.*

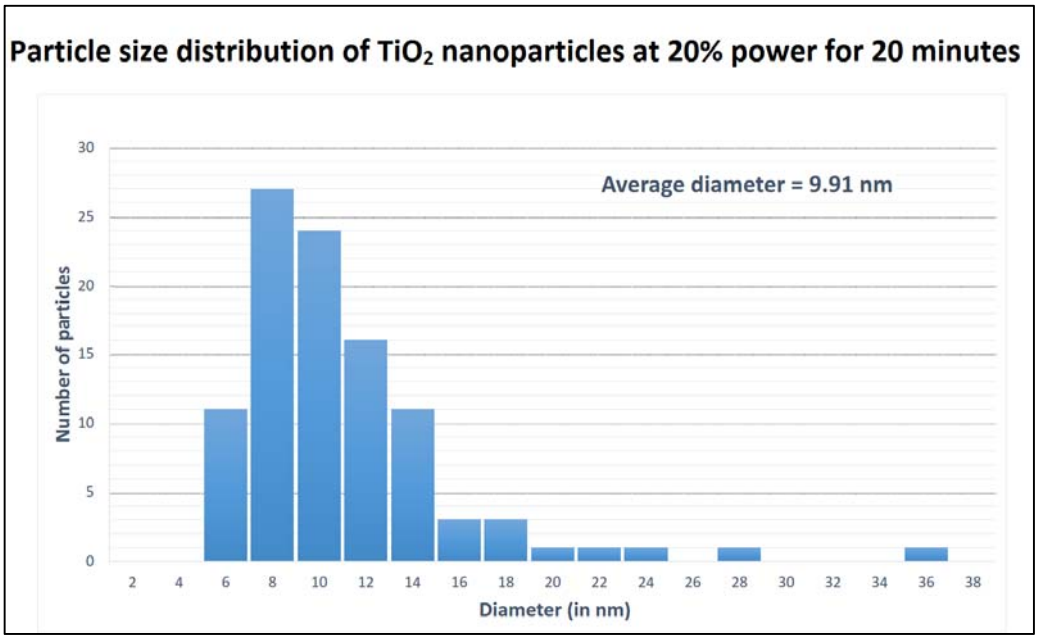

Figure 4.31 *Histogram corresponding to the TEM image of 20% power and 20 minutes ablation time suspension showing the particle size distribution. The average diameter was 9.91 nm.*

From the histogram in figure 4.31, the average diameter of the nanoparticles was calculated to be 9.91 nm. For the same sample, SAXS measurements calculated the average radius to be 8.27 nm. So, the corresponding average diameter was 16.54 nm. But the average value not the only important distribution parameter. Our calculation from TEM image is a number distribution whereas SAXS gives size distribution by volume. The particle size increases as number distribution is converted to volume distribution. The SAXS figure 4.32 shows most frequent particle radius to be 4-5 nanometers which is in line with the TEM histogram in figure 4.31. This could indicate that a lot more particles need to be measured and from the TEM images taken at several different locations on the TEM sample grid. The difference might also be due to the fact that the TEM samples were prepared right after ablation experiment was over whereas the SAXS measurements were carried out several hours and in some cases several days after the ablation experiment was done. Due to this time lag, there is possibility of agglomeration, in which case the SAXS might not be able to detect the primary particle size. In addition, the amorphous phase that surrounds the particles may vary the scattering of the x-rays. Due to the presence of amorphous phase (discussed in the TEM section 4.2.1.1), the average measured values from SAXS are about 6.63 nm higher than that measured from TEM images manually. However, it is important to point out that in TEM we are looking at a very small area and there is always a possibility that the small area is not representative of the bulk.

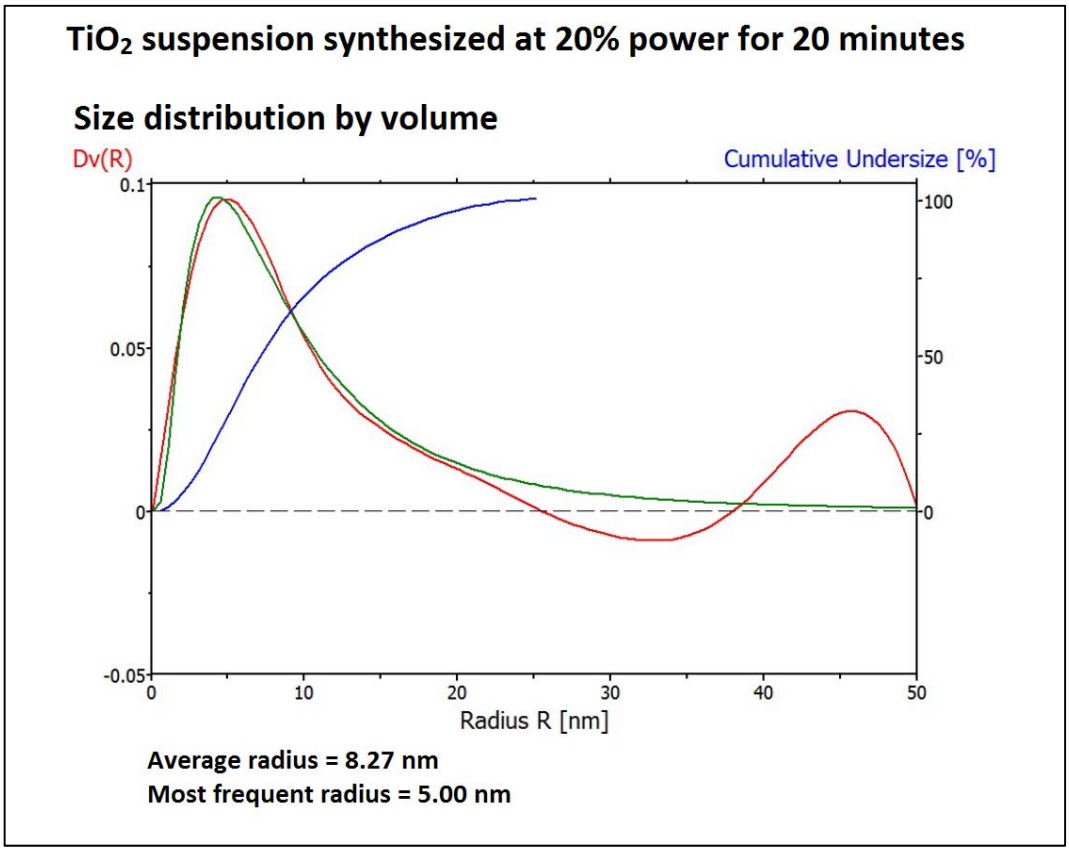

Figure 4.32 *Size distribution measured by small angle x-ray scattering for suspension synthesised at 20% power for 20 minutes.*

Figures 4.33 and 4.34 represent the TEM image and the corresponding size distribution histogram from TEM image for suspension synthesised at 40% laser power and 30 minutes ablation respectively. Figure 4.35 shows the small angle x-ray scattering results of the TiO_2 suspension. The size distribution of nanoparticles calculated from TEM image is compared with the determined by SAXS. The measurements from the TEM image resulted in 7.30 nm average diameter whereas the SAXS measurements resulted in 6.88 nm radius, or 13.76 nm diameter. There is difference in the measured values of the two techniques, however, the differences in the values can be argued to have occurred because of the same reasons mentioned for size distribution measurements of 20% laser power for 20 minutes ablation time sample which was the presence of amorphous phase on particle boundary that varies the scattering of x-rays and agglomeration effects.

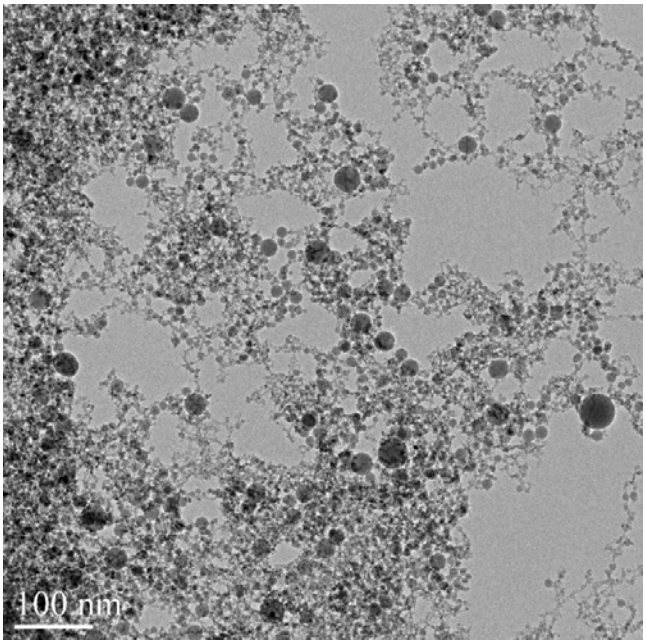

Figure 4.33 *TEM image from 40%, 30 minutes sample which was used to manually measure the particle sizes and form the corresponding histogram*

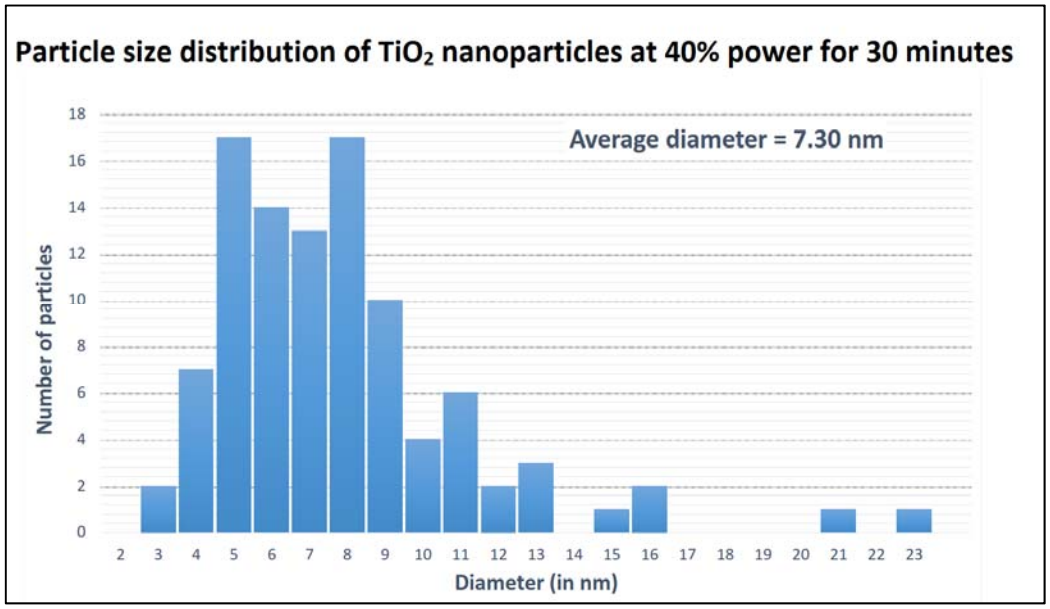

Figure 4.34 *Histogram corresponding to the TEM image of 40% power and 30 minutes ablation time suspension showing the particle size distribution. The average diameter was 7.30 nm.*

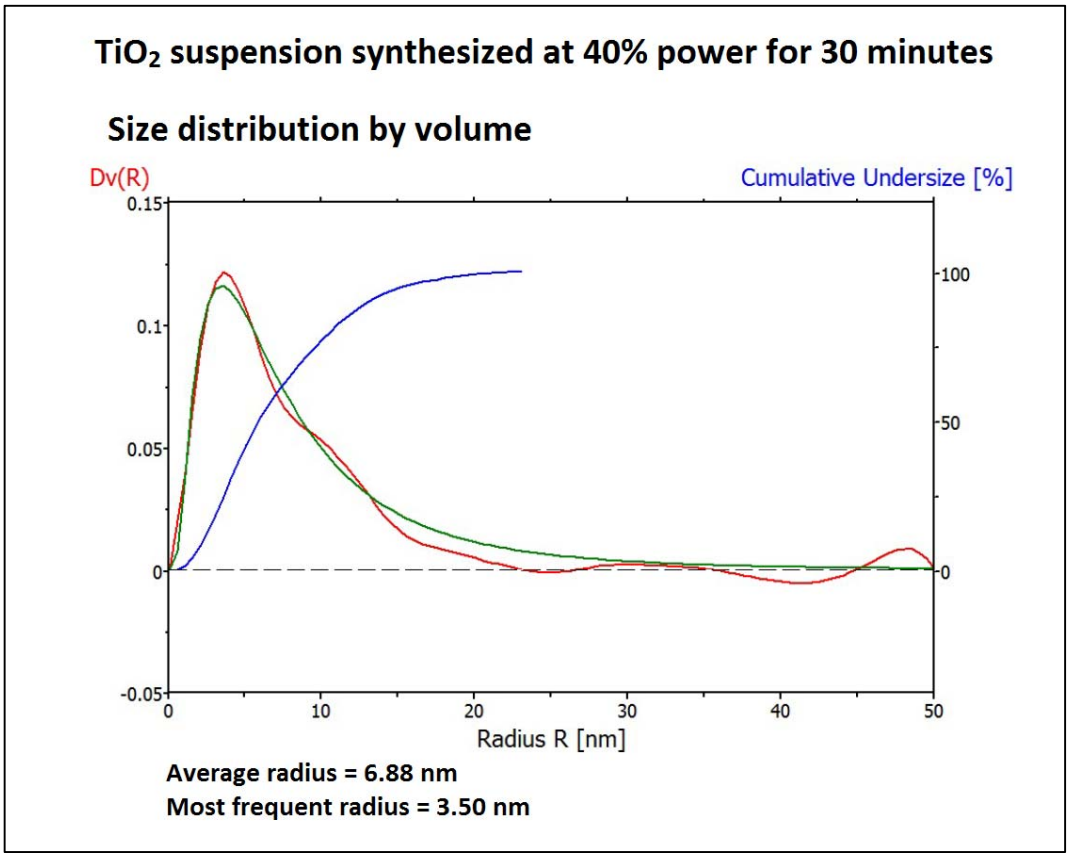

Figure 4.35 *Size distribution measured by small angle x-ray scattering for suspension synthesised at 40% power for 30 minutes.*

Figures 4.36 and 4.37 represent the TEM image and the corresponding size distribution histogram from TEM image for suspension synthesised at 50% laser power and 30 minutes ablation respectively. Figure 4.38 shows the SAXS results from the same sample. The measurements from the TEM image resulted in 6.07 nm average diameter whereas the SAXS measurements resulted in 6.08 nm radius, or 12.16 nm diameter. A similar argument could be proposed for the difference in the values as is done for the previous samples that were synthesised at 20% and 40% laser power and for 20 minutes and 39 minutes ablation time respectively.

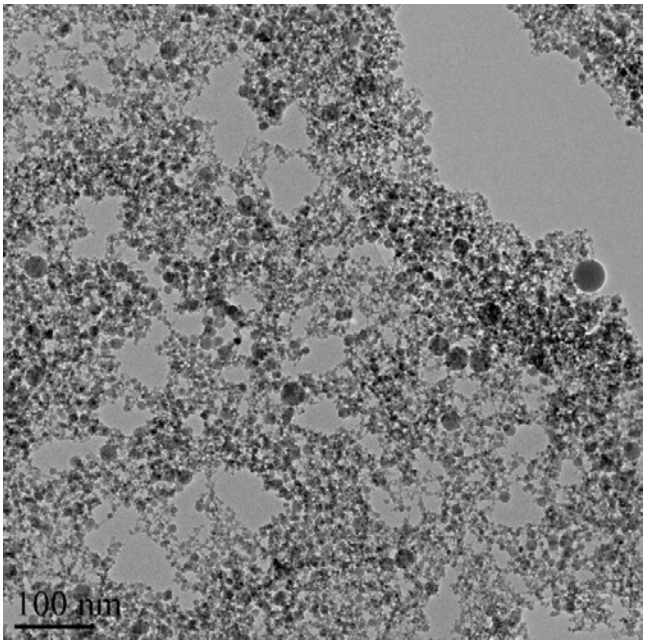

Figure 4.36 *TEM image from 50%, 30 minutes sample which was used to manually measure the particle sizes and form the corresponding histogram*

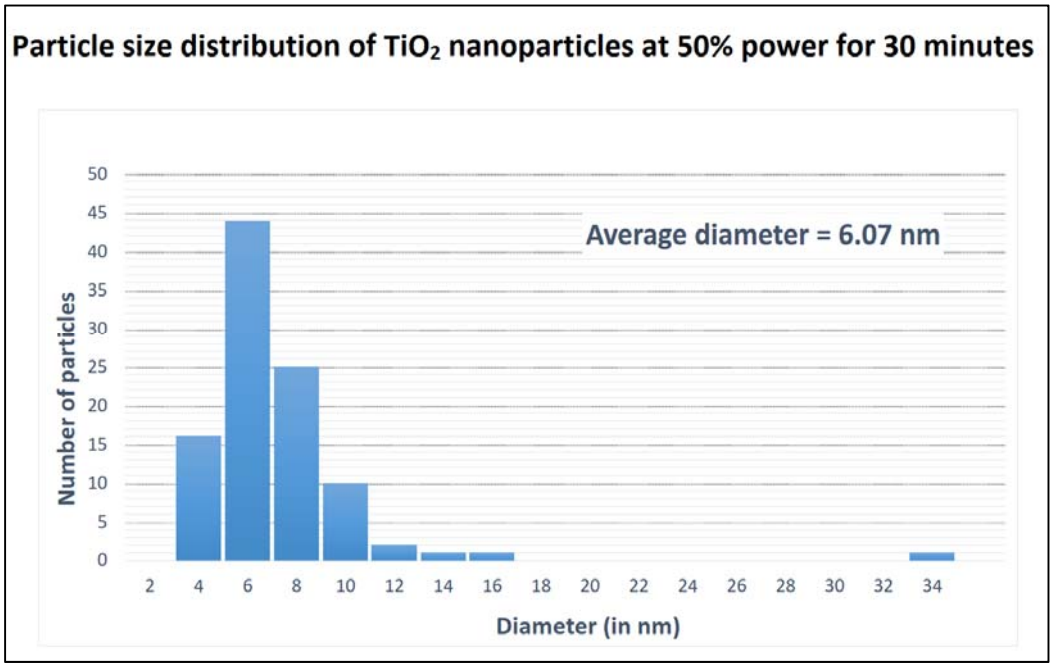

Figure 4.37 *Histogram corresponding to the TEM image of 40% power and 30 minutes ablation time suspension showing the particle size distribution. The average diameter was 7.30 nm.*

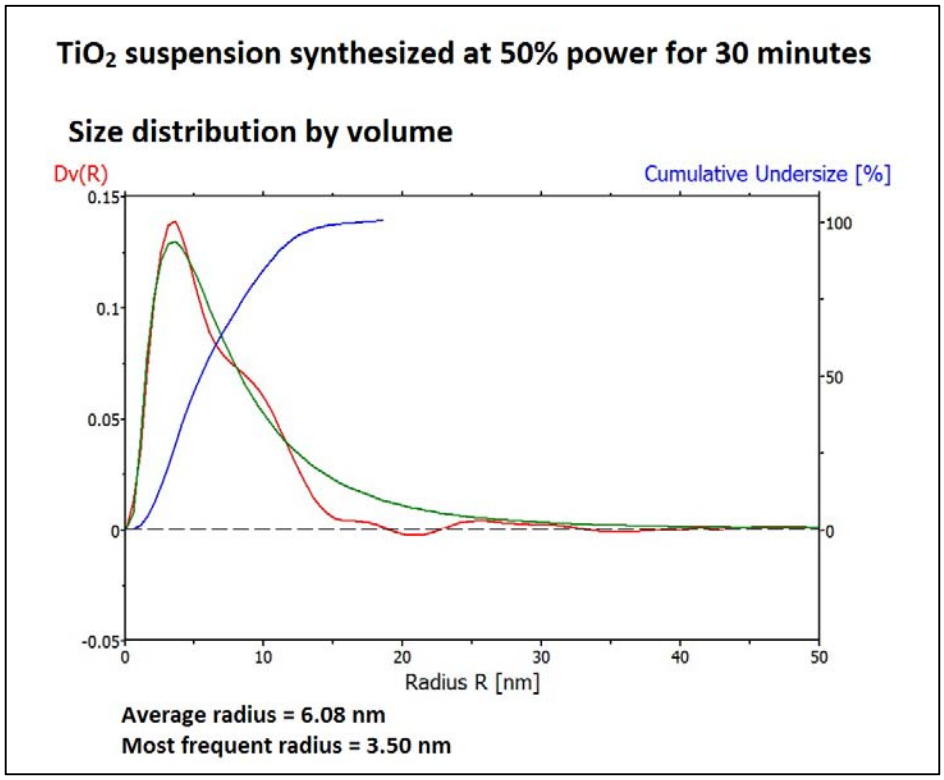

Figure 4.38 *Size distribution measured by small angle x-ray scattering for suspension synthesised at 50% power for 30 minutes.*

Even though the SAXS measurements (figures 4.32, 4.35, and 4.38) are not exactly the same as the TEM measurements but still they show the same trend in the variation of the particle size with the laser power. From the histogram measurements, it can be deduced that the increase in the laser power decreased the average diameter of the nanoparticles. A similar trend is visible in the SAXS measurements. Therefore, we can refer to the SAXS measurements in order to analyse the effect of laser power on the particle size distribution.

Figures 4.39, 4.40, 4.35, 4.38 and 4.41 represent the SAXS measurements for suspensions synthesised at 20%, 30%, 40%, 50% and 60% laser powers and 30 minutes ablation time respectively. Table 4.3 shows the variation of TiO_2 nanoparticle with the laser power. The average radius of the nanoparticles decreased from 20% laser power to 60% laser power for each value of laser power used. The average radius for the corresponding laser powers were 9.92 nm at 20%, 7.57 nm at 30%, 6.88 nm at 40%, 6.08 nm for 50% and 5.71 nm for 60% of the maximum laser power.

Table 4-3 *Variation of TiO_2 nanoparticle size with laser power*

S. No.	Percentage of max. Laser Power [%]	Avg radius of TiO_2 nanoparticle [nm]
1	20%	9.92
2	30%	7.57
3	40%	6.88
4	50%	6.08
5	60%	5.71

One possible reason for the decrease in the size of the nanoparticles is the effect of the laser processing on the particles while the ablation experiment is going on. It is important to remind that the synthesised nanoparticles are stable as a suspension for several hours, and also keeping in mind that the duration of the pulsed laser ablation experiment was 30 minutes in this series of tests. Therefore, the nanoparticles that are ablated when the ablation experiment begins, they are present in the suspension as stable nanoparticles. These nanoparticles interact with the oncoming laser and undergo severe heating from the laser or in other words irradiation of the suspension under laser occurs and the size of the nanoparticles decreases due to evaporation and melting in nanoparticles. These nanoparticles dissociate while they are directly under focussed laser beam. Takami et al. [23] have reported decrease in the particle size due to melting and vaporisation effects induced by laser. The severity of the plasma increases with the increase in laser power which lead to more bubbling in the suspension and the more particles can undergo laser processing. As the laser power increases, the particles that are directly under the laser dissociate to a larger extent as compared to the same particles at lower powers. This is one possibility of the proportional decrease in the size of the nanoparticle with the increase in the laser power keeping all the other parameters constant.

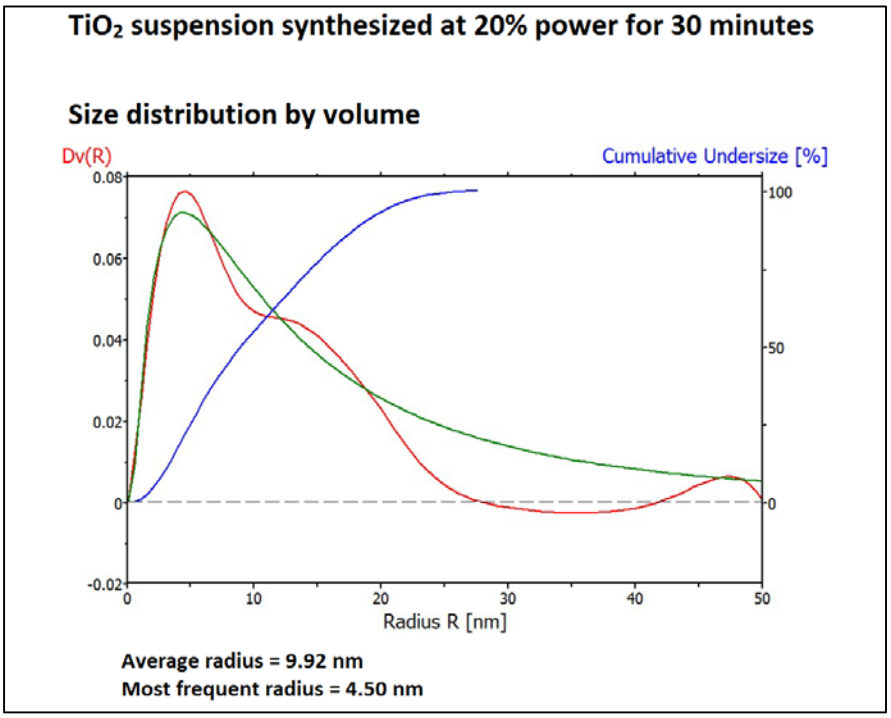

Figure 4.39 *Size distribution measured by small angle x-ray scattering for suspension synthesised at 20% power for 30 minutes*

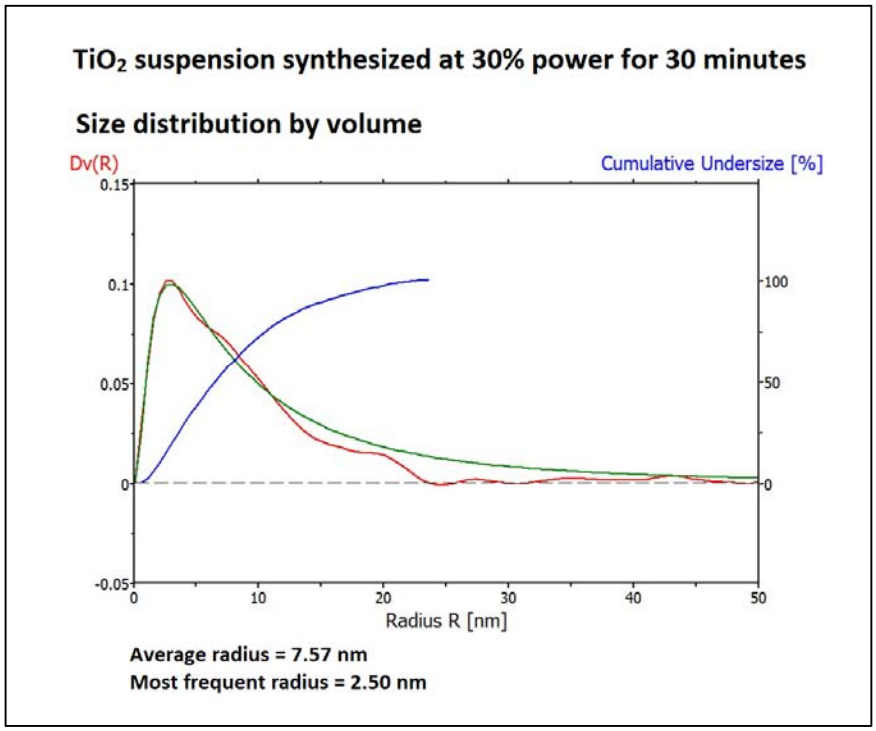

Figure 4.40 *Size distribution measured by small angle x-ray scattering for suspension synthesised at 30% power for 30 minutes.*

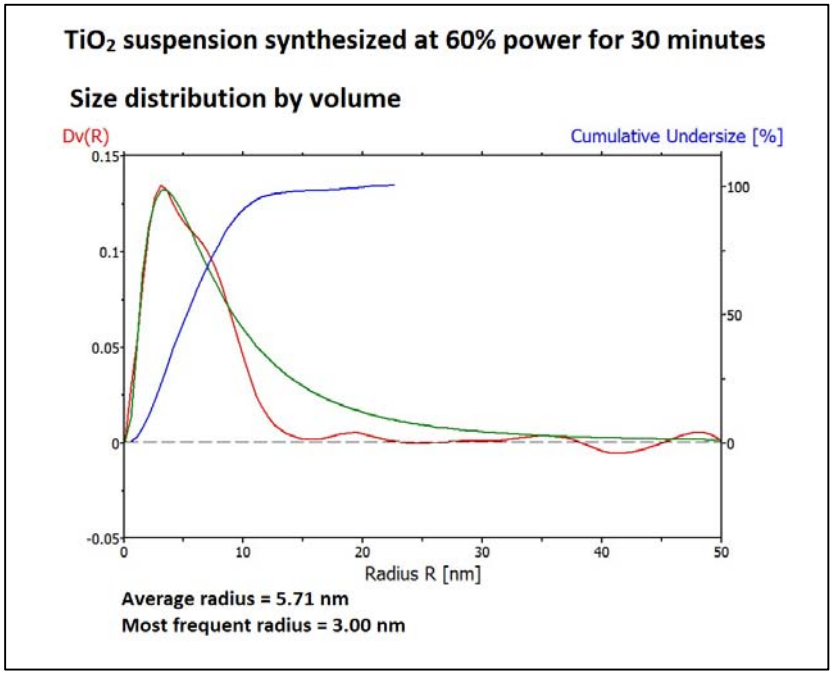

Figure 4.41 *Size distribution measured by small angle x-ray scattering for suspension synthesised at 60% power for 30 minutes*

In addition, the SAXS measurements also indicated the percentage of particles that are smaller than the corresponding radius of the particle on the x-axis.

4.2.4 Surface profiles of ablated target

Optical profilometer was used to characterise irradiated region of the pulsed laser ablated targets. Surface profilometer results from two titanium targets and one graphite target are shown in figures 4.42 – 4.57. These results include the analysis of the ablated target with three different techniques, namely, the 2-D surface profile view, XY profile view and 3-D interactive view.

In the results of each target, firstly the 2-D surface profile is shown which is followed by the 3-D view and then finally the XY profile view. Figure 4.42 shows the 2-D profile of the irradiated titanium target. The right portion in the figure is the ablated region and is deeper than the surrounding region on its left which is the non-ablated region. The colour scale in the right hand side of the figure represents the height (z-axis). So, accordingly the region between the ablated and the non-ablated region is the deepest area in the figure. This is further understood from the 3-D view of the sample. In figure 4.43, the top left part of the target represents the non-ablated region and is higher than the ablated region on the right.

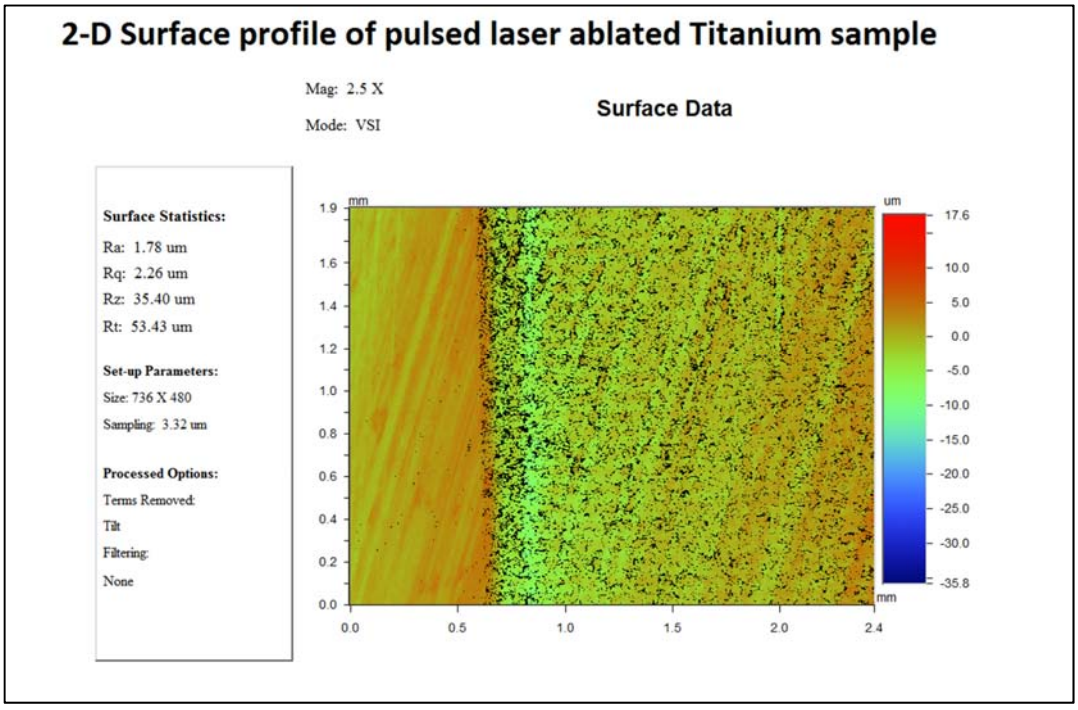

Figure 4.42 *2-D surface profile of pulsed laser ablated titanium target.*

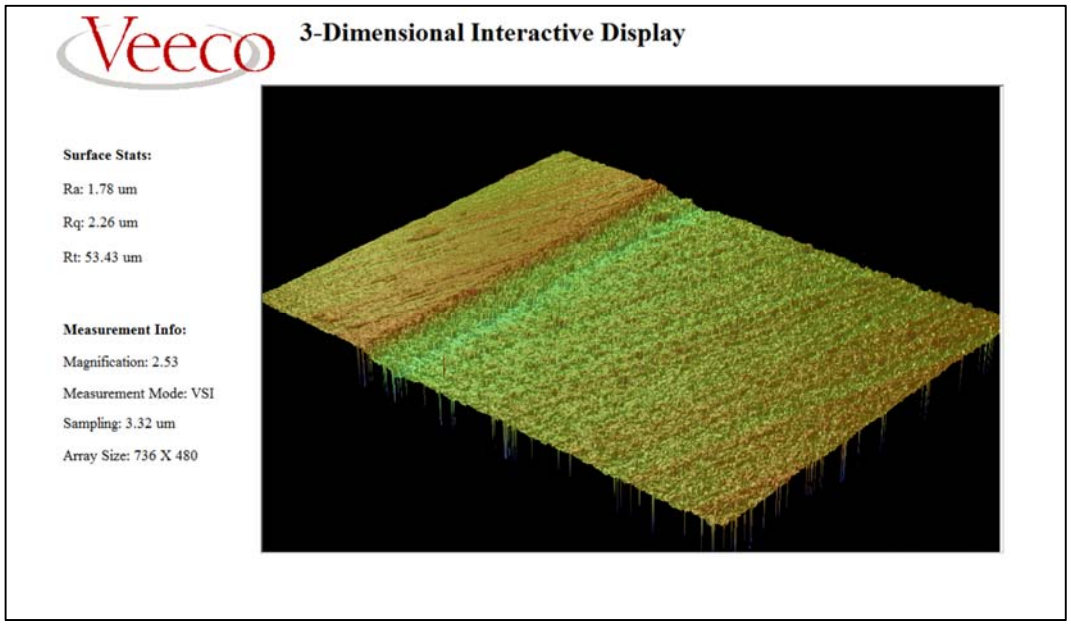

Figure 4.43 *3-Dimensional view of the pulsed laser ablated region in graphite. The top left part of the target represents the non-ablated region and is higher than the ablated region on the right.*

The first two images helped to qualitatively determine the high or low areas of the sample but the XY profile assisted in knowing the depth at the exact chosen points. Figure 4.44 shows the X profile for two chosen points, one at the ablated region and one at the non-ablated region. The difference in the height was 2 µm. There was no difference in the heights of the regions chosen on the Y-axis. Therefore, in that direction, the pulsed laser ablation was uniform. This gave rise to the question how the difference in the heights of the ablated region and non-ablated vary at different points. Clearly from the 2-D and 3-D profiles, it can be noticed that the deepest region is the area just between the ablated and non-ablated region (this deep region is part of the ablated region). Figures 4.45 – 4.48 represent the X-axis profiles of the target. Using these it can be established that the difference in the height where the ablated region ends is ranges between 7.2 µm and 10.9 µm. So, it is not uniform. This tells that the scanning process of the laser during the ablation experiment does not irradiate the edges the same way as it irradiates the centre of the ablated region. However, there is also a possibility that the sample may have been in a slightly tilted position during profile measurement.

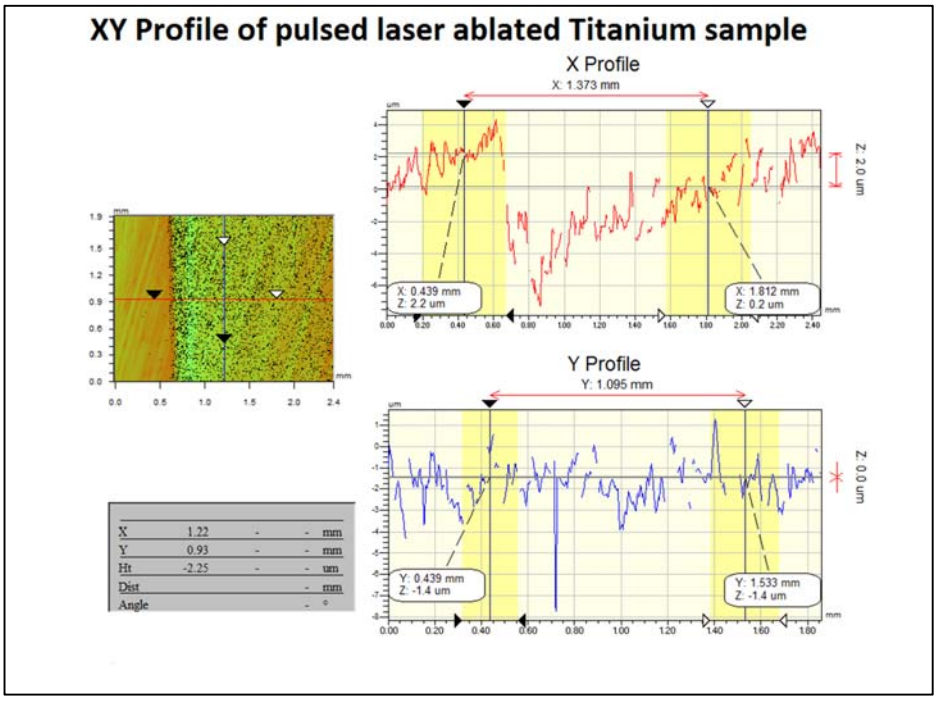

Figure 4.44 *XY profile of the pulsed laser ablated titanium sample*

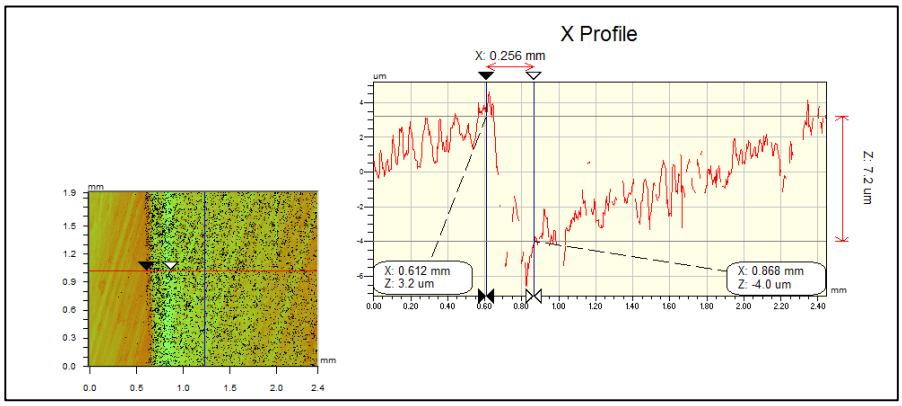

Figure 4.45 *X profile of the pulsed laser ablated titanium target is shown and the difference in the height (z-axis difference) was 7.2 µm.*

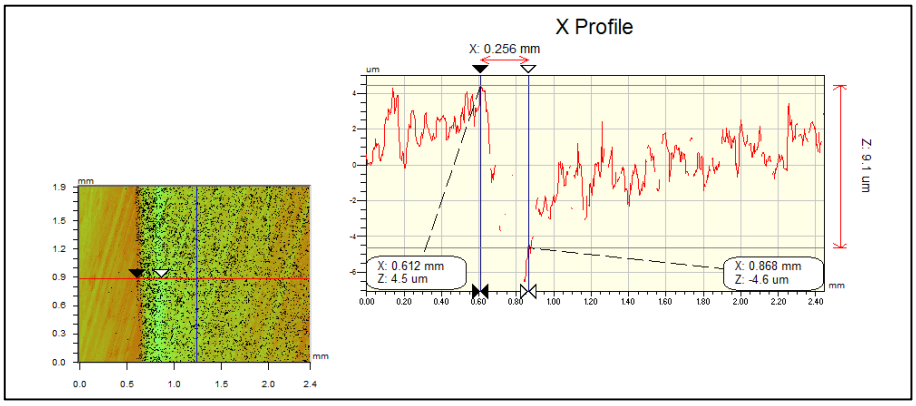

Figure 4.46 *X profiles at two different points shows difference in the z values to be 9.1 µm.*

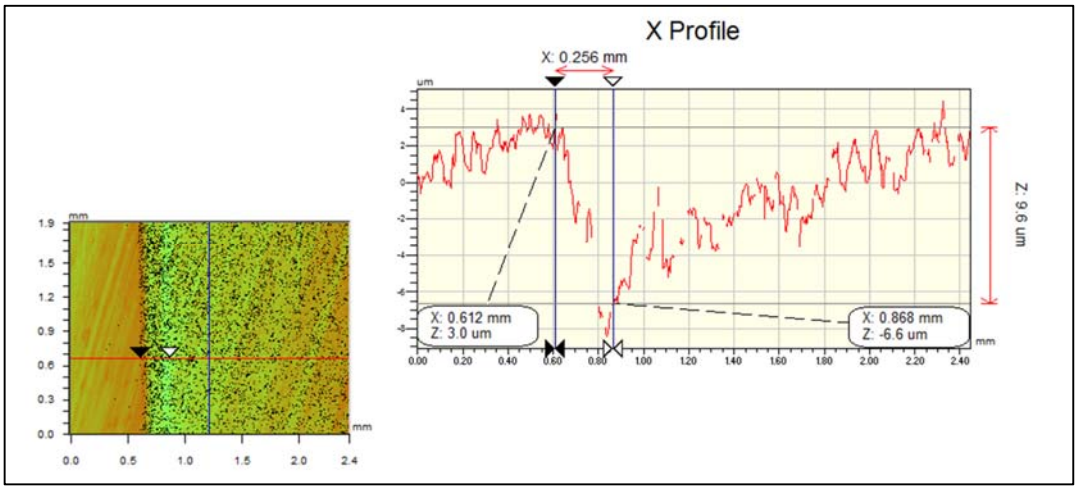

Figure 4.47 *X profile of the pulsed laser ablated titanium target shows the depth of the deepest point to be 9.6 µm at this level on x-axis.*

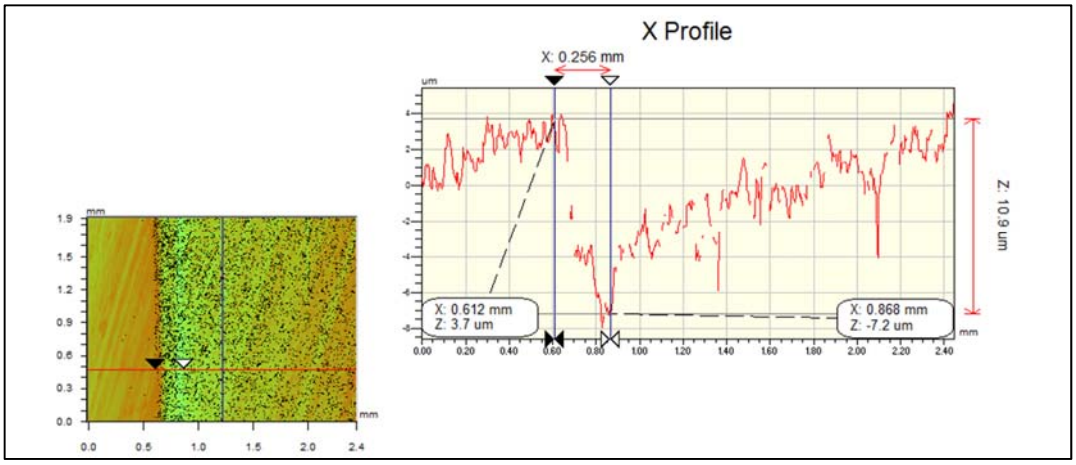

Figure 4.48 *The difference in the z values 10.9 µm is shown in the X profiles at two different points on the laser irradiated target.*

Figures 4.50 and 4.51 show the 2-D profile and 3-D view of the irradiated titanium sample. The upper portion in the figure was the ablated region and was deeper than the surrounding region below it (in the figure) which was not ablated. Figure 4.52 represents the XY profile view of this sample. The blue region in the figure, according to the colour scale, was the deepest area. This was further proved from figure 4.52, where the difference in the height was quantitatively measured to be 13.1 µm.

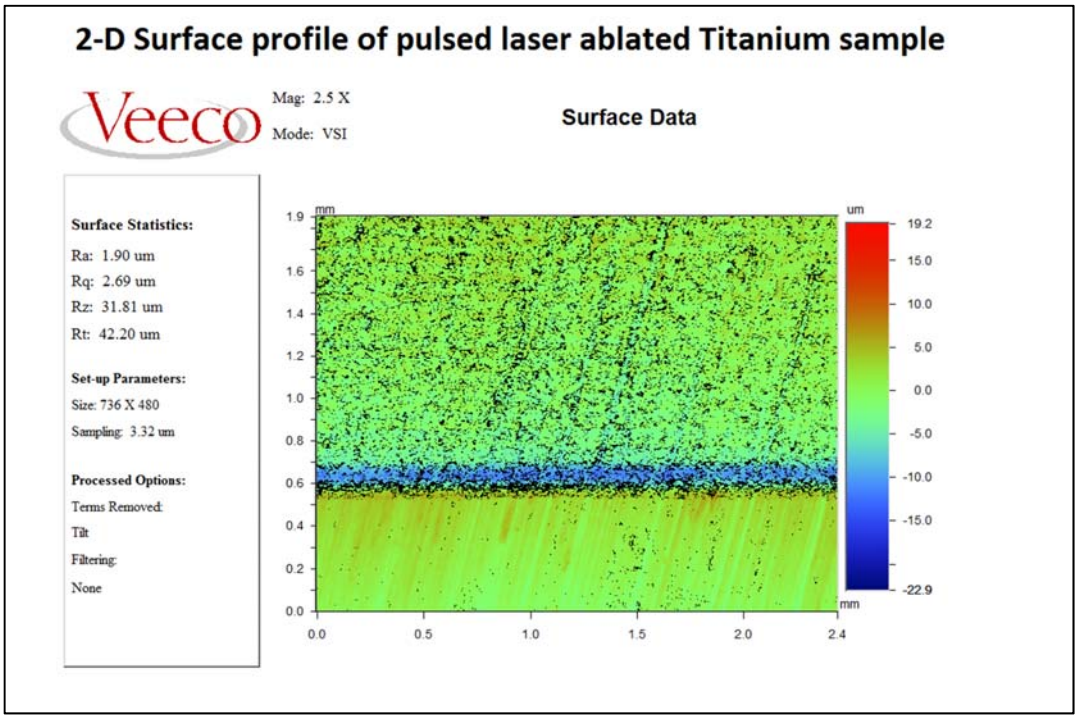

Figure 4.49 *2-D surface profile of pulsed laser ablated titanium sample*

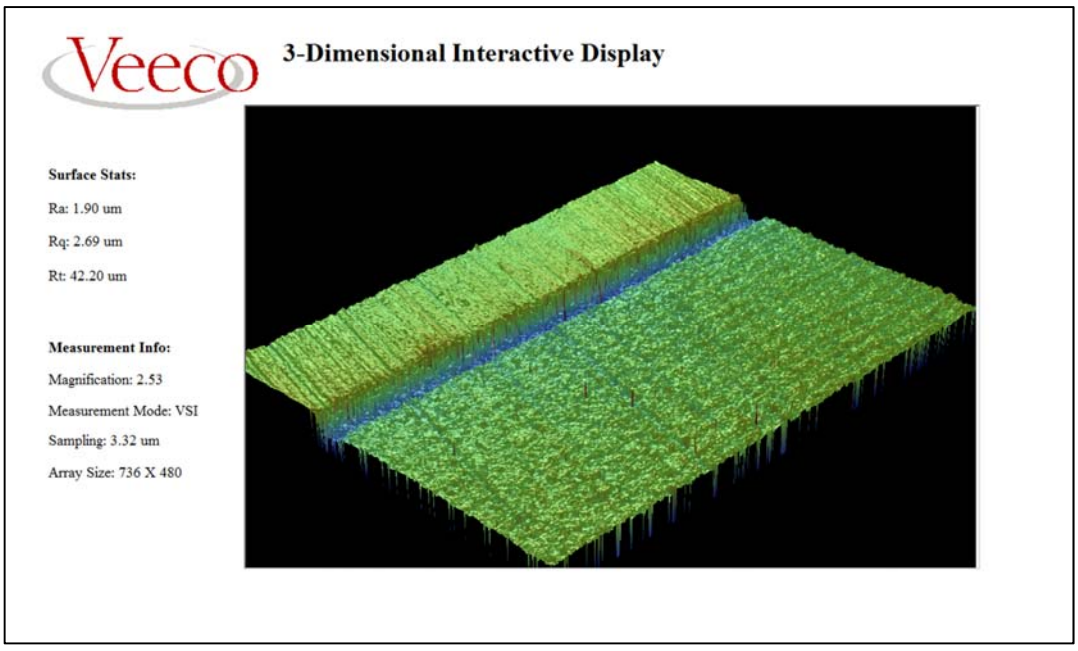

Figure 4.50 *3-Dimensional view of the pulsed laser ablated region in titanium.*

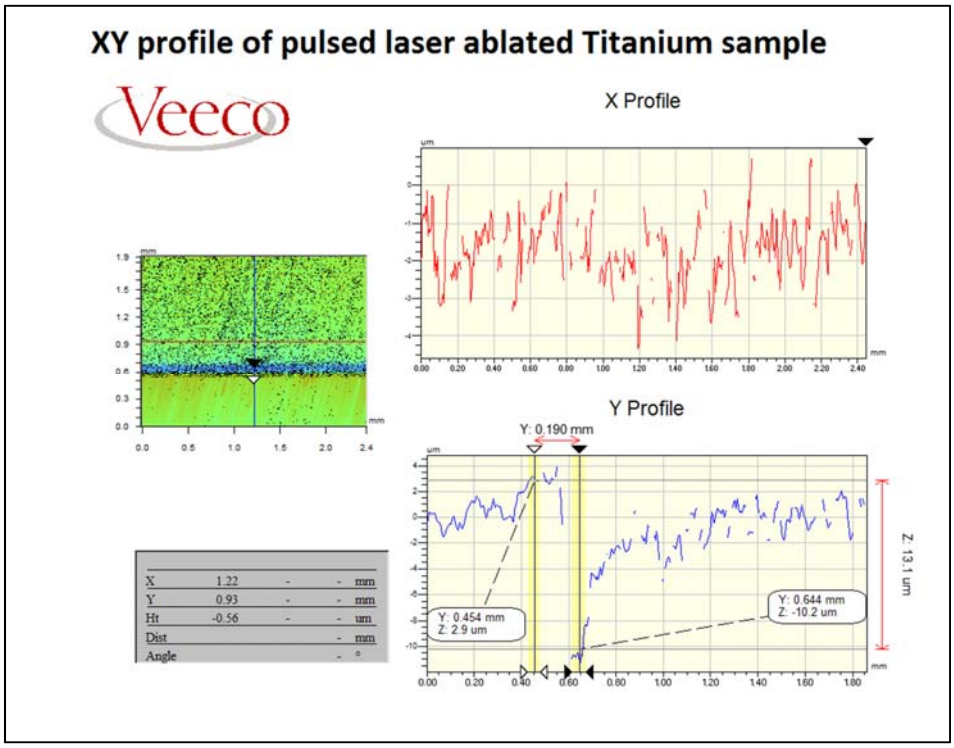

Figure 4.51 *XY profiles at two different points on Y-axis shows difference in the z values between the highest and the deepest parts.*

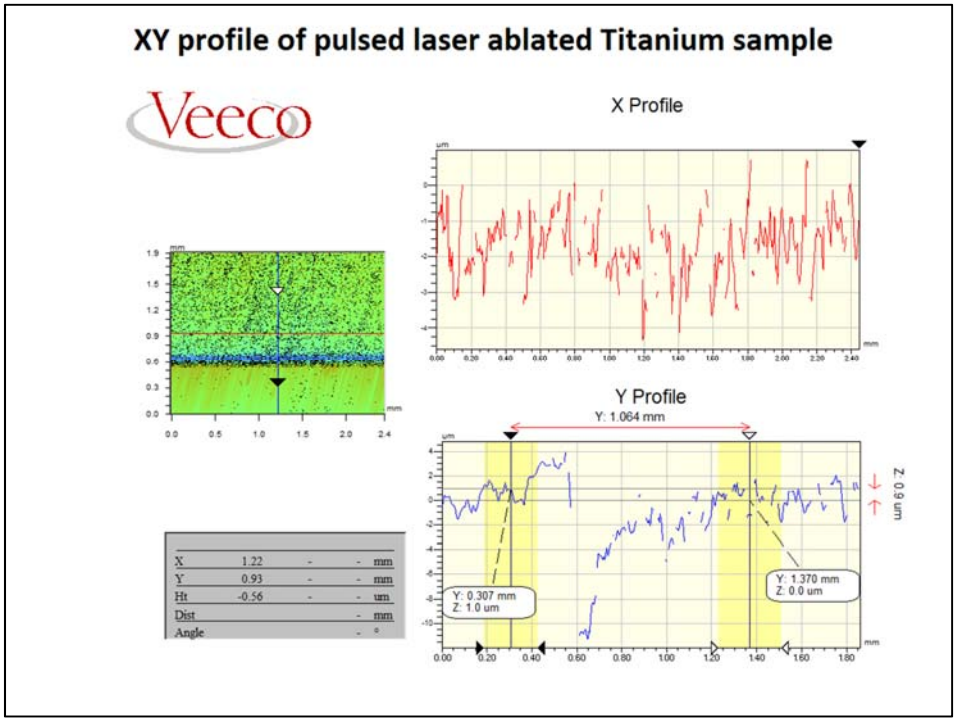

Figure 4.52 *XY profiles at two different points on Y-axis shows difference in the z values of ablated and non-ablated regions.*

The difference between the heights of ablated and non-ablated region was found to be 1 µm at the two chosen points in figure 4.52. There was no variation in the heights on an average with the variation in the x-axis values.

The optical profilometer results for pulsed laser ablated graphite target were also measured in a similar way as the pulsed laser ablated titanium targets. Figure 4.53 and 4.54 show the 2-D and 3-D view of the sample surface. The small blue circles in the 2-dimensional view are the laser spots where the laser pulses hit the sample surface. From the colour calibration with the depth, it was observed that these laser spots were more than 10 µm deeper than the laser ablated region. There was no considerable difference in the colour of the ablated region (on the right hand side) and the non-ablated region (on the left hand side) which implied that the depth of the ablated region is very small.

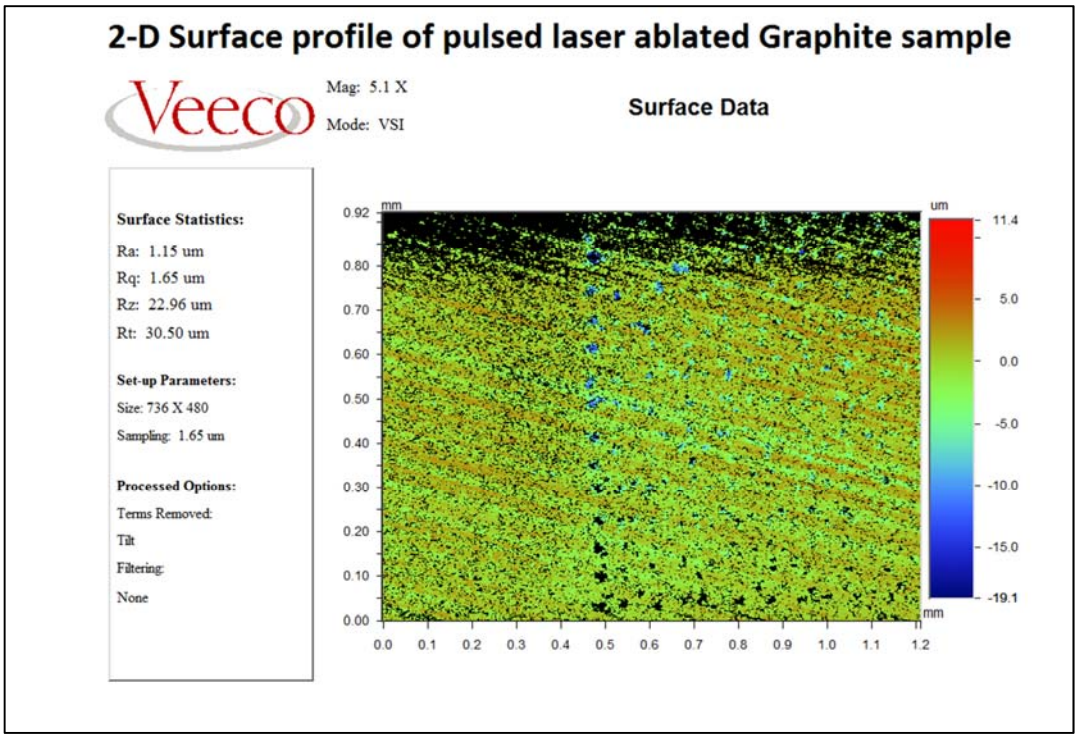

Figure 4.53 *2-D surface profile of pulsed laser ablated graphite sample*

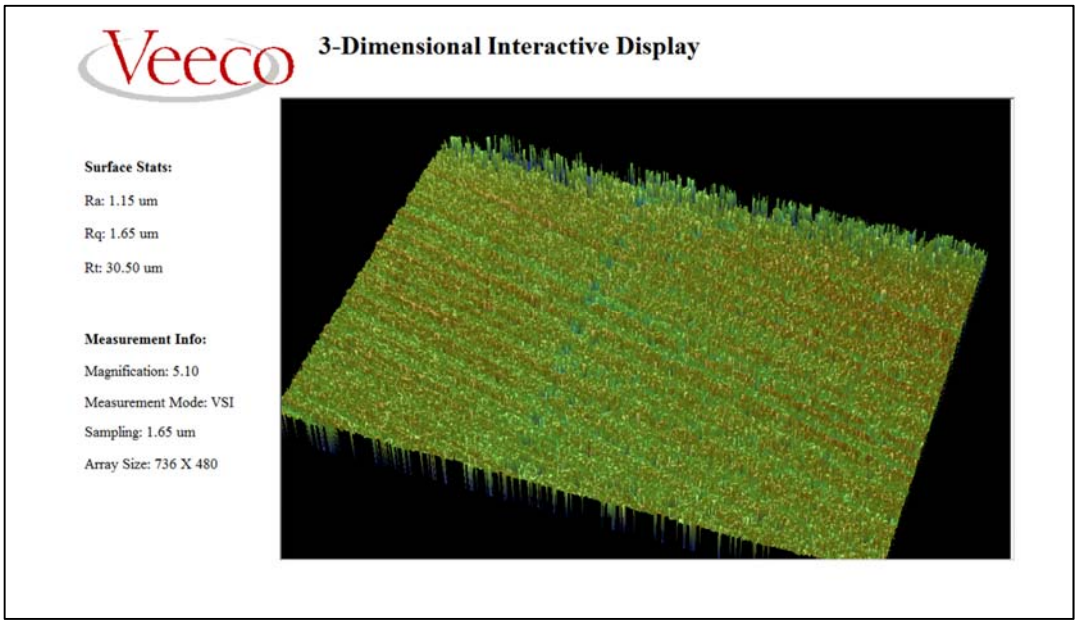

Figure 4.54 *3-Dimensional view of the pulsed laser ablated graphite target.*

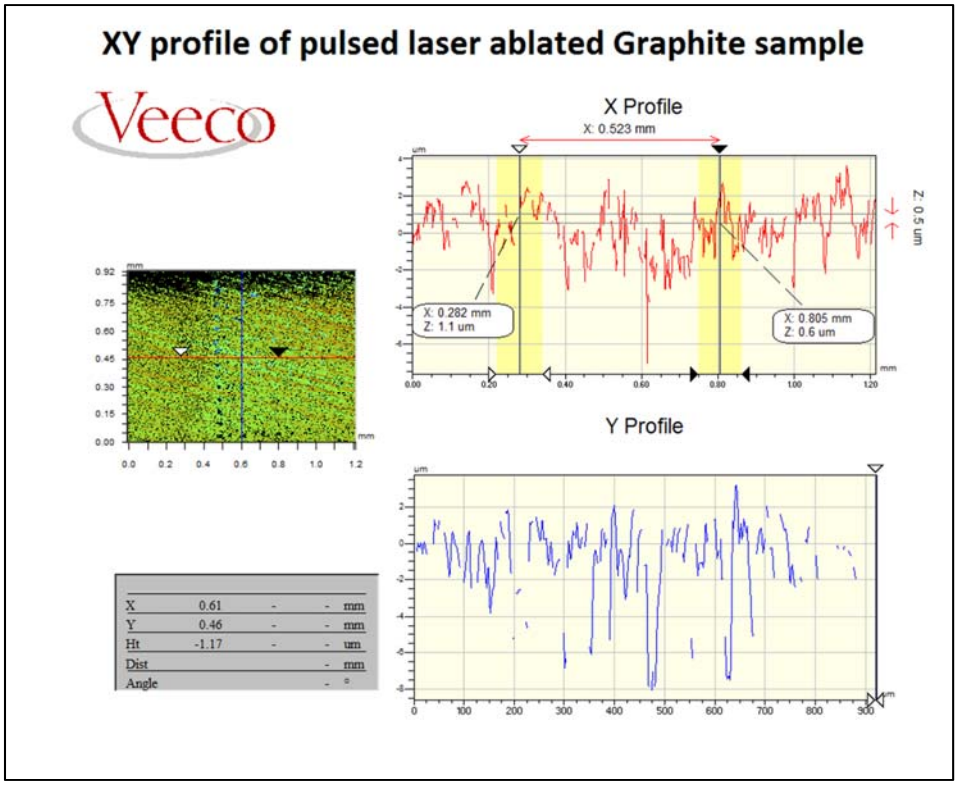

Figure 4.55 *XY profiles at two different points on Y-axis shows difference in the z values of ablated and non-ablated regions.*

Figures 4.56 – 4.58 represent the XY profiles of this sample. From the Y profiles in these figures, it can be established that there was no significant difference in the heights for different values on the y-axis of the ablated region.

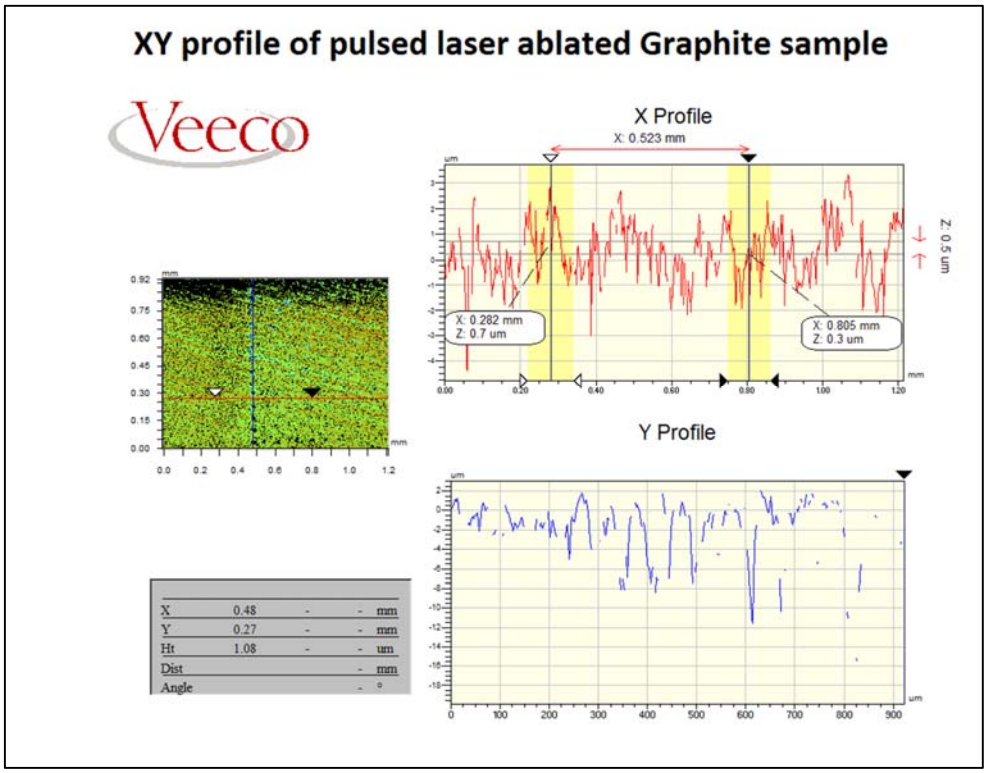

Figure 4.56 *XY profiles at two different points on Y-axis shows difference in the z values of ablated and non-ablated regions.*

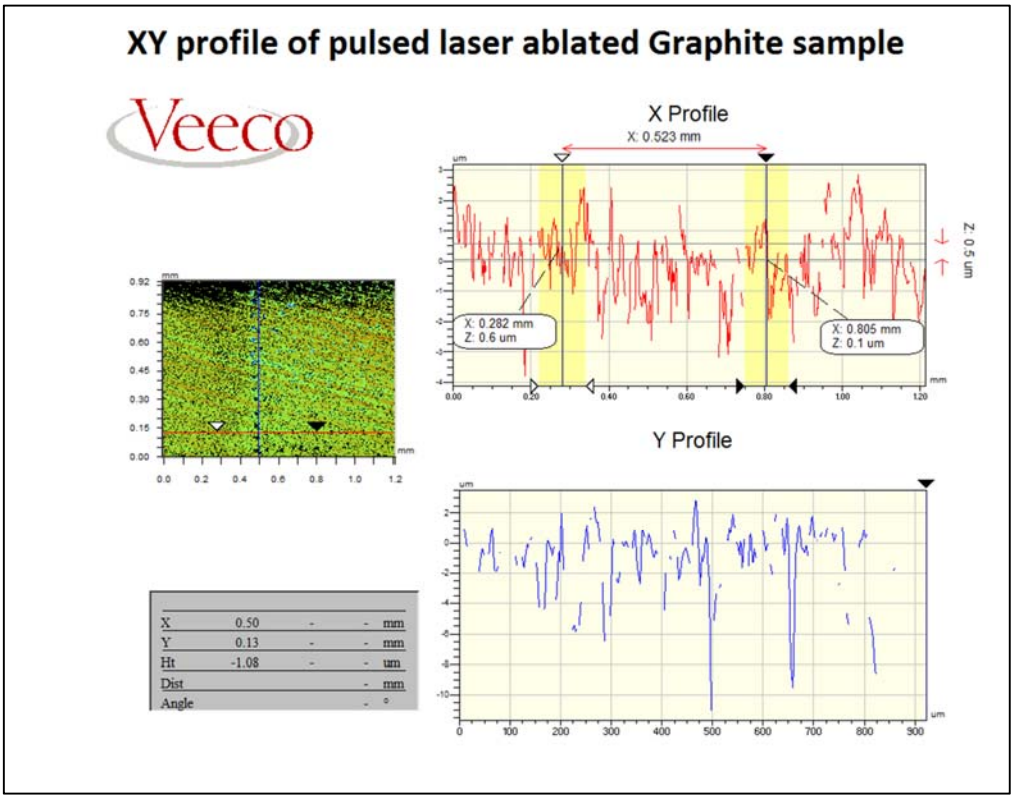

Figure 4.57 *XY profiles at two different points on Y-axis shows difference in the z values of ablated and non-ablated regions*

It could also be established that the depth of the ablated region is uniform and is equal to 500 nm (figures 4.56 – 4.58). This means that the amount of material removed is much smaller than in pulsed laser ablation of titanium. This is in accordance with the weight measurement results mentioned in 4.1.3. The amount of nanoparticles produced by pulsed laser ablation of titanium was several milligrams (1.5 mg to 17 mg in half an hour) which is much higher compared to the only 2 milligrams (maximum 2 mg at 80% laser power, half an hour ablation time) of nanoparticles produced by pulsed laser ablation of graphite. This also implies that the threshold laser fluence needed for graphite is much higher than that needed for titanium. For nanosecond lasers, the threshold laser fluence is proportional to the melting point of the material [14].

5. CONCLUSION

Firstly, in this thesis work, TiO_2 nanoparticles and carbon nanotubes were successfully synthesized by pulsed laser ablation of titanium and graphite targets respectively. The implementation of the pulsed laser ablation experiment was found to be simple and user friendly. In the experimental part of this study, the synthesis of nanoparticles has been demonstrated by pulsed laser ablation of titanium and graphite in deionised water.

For ablated Titanium suspensions, we found that the yield of nanoparticles increases to the point of maximum fluency at 40% of maximum laser power. Then starts to decrease when power is increased to 50% due to decrease in the laser fluence but increased again at 60% power because of cumulative effect of the overlapping laser spots. For ablated graphite suspensions, the yield of carbon nanoparticles was found to be independent of the laser fluence but dependent on the laser power. The yield increased with increasing laser power until solvent effects such as evaporation came into effect.

In the ablation of titanium target, round crystalline nanoparticles were found in the transmission electron microscopy of ablated suspensions and they were surrounded by amorphous phase nanoparticles. The EDS results indicated the presence of titanium and oxygen in the sample. XRD measurements identified the nanoparticles to be TiO_2 that belonged to both anatase and rutile. Wide angle x-ray scattering indicated presence of anatase, rutile and brookite in the samples. In the XRD of the ablated titanium target, we found three different oxides of titanium besides titanium metal itself. The oxides found were titanium monoxide, titanium dioxide and titanium (III) oxide. Titanium dioxide was found to be present as anatase and rutile. The particle size measurements from TEM and SAXS indicated decrease in size of the TiO_2 nanoparticles with the increase in laser power.

In the ablation of the graphite target, TEM results of the suspensions obtained from ablation of graphite indicated presence of carbon nanotubes. Further analysis with XRD and WAXS could not be done for the corresponding dried suspension as the quantity was insufficient. However, on the surface of the ablated graphite target, we found diamond with XRD.

The surface profile measurements of ablated titanium target indicated non-uniformity of the laser scanning process. The deepest point in the ablated region was measured to be 13.1 μm. The surface profile measurements for ablated graphite measured the depth of the pulsed laser ablated region to be 500 nm.

Further work on liquid phase pulsed laser ablation would include similar ablation experiments inside high pressure chamber. It would be interesting to compare these results with similar tests performed in supercritical fluids such as in supercritical carbon dioxide. With supercritical fluids, the better control on the synthesis process is one of its biggest advantages. Moreover, with a small decrease in pressure supercritical carbon dioxide

could be made to leave the system like a gas without leaving any residue. Functionalization of the synthesised nanoparticles is also a very hot topic in the field of science these days and is recommended as future scope of work for this study.

REFERENCES

[1] K. S. Novoselov et al., “Electric field effect in atomically thin carbon films.,” *Science (New York, N.Y.)*, vol. 306, no. 5696, pp. 666–9, Oct. 2004.

[2] Global Nanomaterials Market-Market Size, Demand and Forecasts to 2016. Accessed on 03.10.2014 from http://www.academia.edu/6413132/Global_Nanomaterials_Market-Market_Size_Demand_and_Forecasts_to_2016

[3] Graphene Markets, Technologies and Opportunities 2014-2024. Accessed on 03.10.2014 from http://www.idtechex.com/research/reports/graphene-markets-technologies-and-opportunities-2014-2024-000390.asp

[4] A. Zurutuza and C. Marinelli, “Challenges and opportunities in graphene commercialization.,” *Nature nanotechnology*, vol. 9, no. 10, pp. 730–734, Oct. 2014.

[5] T. Sasaki, Y. Shimizu, and N. Koshizaki, “Preparation of metal oxide-based nanomaterials using nanosecond pulsed laser ablation in liquids,” *Journal of Photochemistry and Photobiology A: Chemistry*, vol. 182, no. 3, pp. 335–341, Sep. 2006.

[6] K. Urabe et al., “Dynamics of pulsed laser ablation in high-density carbon dioxide including supercritical fluid state,” *Journal of Applied Physics*, vol. 114, no. 14, p. 143303, 2013.

[7] S. Machmudah, N. Takada, H. Kanda, K. Sasaki, and M. Goto, “Fabrication of gold and silver nanoparticles with pulsed laser ablation under pressurized CO 2,” *Advances in Natural Sciences: Nanoscience and Nanotechnology*, vol. 4, no. 4, p. 045011, Oct. 2013.

[8] K. Saitow, T. Yamamura, and T. Minami, “Gold nanospheres and nanonecklaces generated by laser ablation in supercritical fluid,” *The Journal of Physical Chemistry C*, vol. 112, pp. 18340–18349, 2008.

[9] S. Machmudah, Y. Kuwahara, M. Sasaki, and M. Goto, “Nano-structured particles production using pulsed laser ablation of gold plate in supercritical CO2,” *The Journal of Supercritical Fluids*, vol. 60, pp. 63–68, Dec. 2011.

[10] Z. Yan and D. B. Chrisey, “Pulsed laser ablation in liquid for micro-/nanostructure generation,” *Journal of Photochemistry and Photobiology C: Photochemistry Reviews*, vol. 13, no. 3, pp. 204–223, Sep. 2012.

[11] S. Dolgaev, A. Simakin, and V. Voronov, “Nanoparticles produced by laser ablation of solids in liquid environment,” *Applied Surface Science*, vol. 186, pp. 546–551, 2002.

[12] N. G. Semaltianos et al., “Laser ablation in water: A route to synthesize nanoparticles of titanium monoxide,” *Chemical Physics Letters*, vol. 496, no. 1–3, pp. 113–116, Aug. 2010.

[13] L. Yang, P. W. May, L. Yin, J. a. Smith, and K. N. Rosser, “Growth of diamond nanocrystals by pulsed laser ablation of graphite in liquid,” *Diamond and Related Materials*, vol. 16, no. 4–7, pp. 725–729, Apr. 2007.

[14] T. Salminen, “Production of Nanomaterials by Pulsed Laser Ablation,” Tampere University of Technology, 2013.

[15] D. Amans et al., “Nanodiamond synthesis by pulsed laser ablation in liquids,” *Diamond and Related Materials*, vol. 18, no. 2–3, pp. 177–180, Feb. 2009.

[16] A. Al-Hamaoy et al., “Liquid Phase – Pulsed Laser Ablation: A route to fabricate different carbon nanostructures,” *Applied Surface Science*, vol. 302, pp. 141–144, May. 2014.

[17] S. Nakahara, S. Stauss, T. Kato, T. Sasaki, and K. Terashima, “Synthesis of higher diamondoids by pulsed laser ablation plasmas in supercritical CO2,” *Journal of Applied Physics*, vol. 109, no. 12, p. 123304 (1–8), 2011.

[18] P. V. Kazakevich, a. V. Simakin, V. V. Voronov, and G. a. Shafeev, “Laser induced synthesis of nanoparticles in liquids,” *Applied Surface Science*, vol. 252, no. 13, pp. 4373–4380, Apr. 2006.

[19] R. K. Thareja and S. Shukla, “Synthesis and characterization of zinc oxide nanoparticles by laser ablation of zinc in liquid,” *Applied Surface Science*, vol. 253, no. 22, pp. 8889–8895, Sep. 2007.

[20] T. Kato et al., “Pulsed laser ablation plasmas generated in CO2 under high-pressure conditions up to supercritical fluid,” *Applied Physics Letters*, vol. 101, no. 22, p. 224103, 2012.

[21] S. Ibrahimkutty, P. Wagener, A. Menzel, A. Plech, and S. Barcikowski, “Nanoparticle formation in a cavitation bubble after pulsed laser ablation in liquid studied with high time resolution small angle x-ray scattering,” *Applied Physics Letters*, vol. 101, no. 10, p. 103104, 2012.

[22] N. Takada and S. Machmudah, “Characteristics of optical emission intensities and bubblelike phenomena induced by laser ablation in supercritical fluids,” *Japanese Journal of Applied Physics*, vol. 010213, 2014.

[23] A. Takami, H. Kurita, and S. Koda, “Laser-induced size reduction of noble metal particles,” *The Journal of Physical Chemistry B*, vol. 103, no. 8, pp. 1226–1232, 1999.

[24] M. S. Tillack, D. W. Blair, and S. S. Harilal, “The effect of ionization on cluster formation in laser ablation plumes,” *Nanotechnology*, vol. 15, no. 3, p. 390, 2004.

[25] R. Buonsanti et al., “Nonhydrolytic synthesis of high-quality anisotropically shaped brookite TiO2 nanocrystals.,” *Journal of the American Chemical Society*, vol. 130, no. 33, pp. 11223–33, Aug. 2008.